國立中山大學材料與光電科學學系

碩士論文

Department of Materials and Optoelectronic Science

National Sun Yat-sen University

Master Thesis

以去合金法製造多孔金屬玻璃之材料製備與特性分析

**Fabrication and characterization of metallic glass foams
by dealloying method**

研究生：林維昭

Wei-jau Lin

指導教授：黃志青 博士

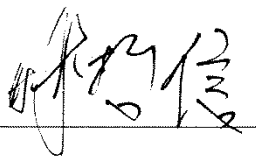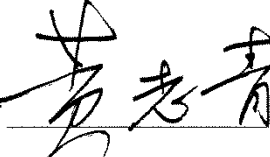Dr. J. C. Huang

中華民國 101 年 7 月

July 2012

國立中山大學研究生學位論文審定書

本校材料與光電科學學系碩士班

研究生林維昭 (學號：M993100040) 所提論文

以去合金法製造多孔金屬玻璃之材料製備與特性分析
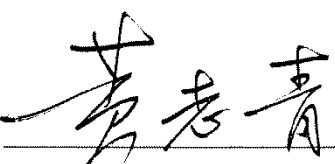Fabrication and characterization of metallic glass foams by dealloying method

於中華民國 *101* 年 *7* 月 *24* 日經本委員會審查並舉行口試，符合碩士學位論文標準。

學位考試委員簽章：

召集人 林哲信 _____   委　員 黃志青 _____

委　員 陳崇桓 _____   委　員 _____

委　員 _____   委　員 _____

指導教授(黃志青) _____ (簽名)

致謝

　　已經在這美麗的西子灣大學度過了四分之一的人生，可以說這裡算是我的第二個家鄉，雖說人終究還是要離家拼搏，只是離別前，這六年來的點滴回憶湧上心頭還是會讓我感到不捨與傷感。而這麼多年來，遇到許多不同的人事物讓我學習到了許多，其中最令我深刻感受的是研究所這兩年。首先要感謝指導教授黃志青教授，帶領我慢慢瞭解金屬玻璃這塊領域並且指導我的實驗，提供許多寶貴的建議，還讓我參與舉辦於香港的國際研討會，研究之外老師對於我們生活近況也十分關心，時常令人窩心與感動，覺得能作為老師的研究生是人生一大幸事，非常感謝老師這兩年來的指導與關照！另外要感謝我的口試委員林哲信教授和陳崇桓教授，以及我的論文計畫口試委員轟台岡教授，他們給了許多研究上的方向與建議，讓我的實驗有今日的成果，論文內容也能更完善。

　　接著感謝實驗室的各個成員，在我這研究生生涯兩年間幫了許多忙。博士後研究員敬仁學長嚴謹的實驗態度與對實驗的熱誠一直是我們的榜樣，另一位博士後研究員育誠學長則是像個萬事通，熱心而且無所不知，謝謝兩位學長在我的研究前期提供了許多寶貴的建議。謝謝鴻升學長和聖堯學長在我碩一時帶著我做實驗，教我使用儀器並且提供建議與方向。名哲學長與浩然學長熱心且風趣，常適時的關心實驗室成員並帶給實驗室歡樂氣氛，對我除了實驗上給予幫助外也教了許多論文的寫作技巧，口試前還幫忙我訂正投影片的錯誤，非常感謝！謝謝哲男學長在研究後期幫我解決了許多實驗上的問題也給了很多想法與建議，大豪學長的生活態度與自我要求也是我學習的對象。朝先學長的研究領域與我相關，與他討論實驗讓我對我的研究更為了解，我的論文有很大一部分要歸功於他。同期進實驗室的同學盈翰室長，謝謝這兩年來課業上的幫忙和生活上的照顧，預祝實驗順利！同屆但資歷比我深的婷婷學姊，感謝你走在我前頭提供我些過來人的經驗。謝謝熱心的瀚生學長也提供了些畢業注意事項與實驗上的建議。感謝學弟妹中瀚、

家驊、詠渝、武漢在我口試時幫忙準備器材與茶點，平時在實驗室也受你們很多照顧。再來要謝謝老同學班代和郭嘉，在家無聊時和你們聊天解悶，也常常給我鼓勵。

　　最後，要謝謝我的父母和家人，在學業與生活方面時常給我許多關心與建議，在我煩躁時包容我的任性，沒有你們在背後的支持我是無法完成學業的。謝謝你們！

Content

List of Tables and Figures

中文摘要

　　本實驗利用去合金法腐蝕方法製備多孔的金屬玻璃薄膜與塊狀金屬玻璃。金屬玻璃薄膜的製備是利用 ZrCuTi 合金靶與純 Ta 靶共濺鍍而成，而塊狀金屬玻璃的製備則是採用兩種成分的金屬玻璃粉末, $Zr_{53}Cu_{30}Ni_9Al_8$ 和 $Ti_{40}Cu_{36}Pd_{14}Zr_{10}$，將 Zr 基與 Ti 基金屬玻璃粉末於此兩種材料重疊的過冷區間溫度燒結。為了製備多孔性的結構，將材料利用 0.1 莫爾濃度的硝酸水溶液經由電化學處理作選擇性腐蝕來製成，材料腐蝕後其金屬玻璃的性質與表面形貌可利用 X 光繞射與掃描式電子顯微鏡作觀測。近來的研究製出了孔洞大小約 10~30 微米，孔洞率為 43%的多孔性金屬玻璃。將來改變粉末大小與體積分率可分別將孔洞大小提升至 300~500 微米，孔洞率提升至 70~80%左右。

關鍵字：金屬玻璃、去合金法、電化學、共濺鍍、多孔

Abstract

The processing and characterization of thin film metallic glasses (TFMGs) and bulk metallic glass foams (BMGFs), prepared by the dealloying corrosion process, have been studied. The TFMGs were fabricated by the co-sputtering with the $Zr_{65}Cu_{25}Ti_{10}$ (wt%) alloy target and the pure Ta target. For BMG, there are two kinds of amorphous metallic powders adopted, namely, $Zr_{53}Cu_{30}Ni_9Al_8$, and $Ti_{40}Cu_{36}Pd_{14}Zr_{10}$. The Zr- and Ti-based powders were sintered at the temperature that Zr- and Ti-based powders overlap their supercooled regions. To fabricate the porous structure, these materials were selectively dissolved using electrochemical treatments in 0.1 M HNO_3 solution. The glassy nature and the pore morphology of the corroded materials were confirmed by X-ray diffraction and scanning electron microscopy. In the current study, the pore size is about 10-30 μm and the porosity volume faction is about 43%. By using different combinations of the powders size and volume fraction, the resulting pore size and porosity fraction can be upgraded to 200-500 μm and 60-80%, respectively.

Keywords: metallic glass, dealloying, electrochemiscal, co-sputtering, porous

Chapter 1 Introduction

1-1 Amorphous alloys or metallic glasses

Amorphous alloys, or termed as metallic glasses, have been developed for very long time, exhibiting unique characteristics, such as good corrosion resistance, high strength and larger elastic energy storage [1]. The reason in causing these characteristics is the random or disordered atomic structure. In contrast to crystalline alloys, which have a highly ordered or long range ordered arrangement of atoms, amorphous alloys are non-crystalline. The atomic structure of amorphous alloys and crystalline materials are shown in Figure 1-1 [2]. The lack of crystalline structure means no crystal defects, such as grain boundaries and dislocations. Due to no crystal defect, amorphous alloys can exhibit special thermal, soft-magnetic and chemical properties.

Amorphous alloys can be applied as biomedical materials, like scalpel and others. Some researches indicated that amorphous alloys have great biocompatibility and mechanical properties. There is a survey [3] indicating that there are about one million surgery cases of the organic replacement per year, and the demand is rising constantly. The applications of amorphous alloys (or metallic glasses) on bio-implant is worthy of further research and

development.

There are many methods to fabricate amorphous alloys, such as vacuum sputtering [4], solid-state reaction [5], chemical vapor deposition or liquid quenching, as described below.

Vacuum sputtering has the highest cooling rate about $10^{10}\sim 10^{12}$ K/s. Therefore, it can be used to fabricate amorphous thin film. Vacuum sputtering can be alone via direct current (DC) sputtering and radio frequency (RF) sputtering by the difference of the power source.

Chemical vapor deposition is a common method to prepare inorganic amorphous thin films, and is widely applied in integrated circuit process. In this process, the wafer (substrate) is exposed to one or more volatile precursors, which react and/or decompose on the surface of substrate to produce the desired deposit. Frequently, volatile by-products are also produced, which are removed by gas flow through the reaction chamber.

Solid-state reaction is meant to make the fined-grained material by severe plastic deformation. As the grain size is refined to a certain level less than 2 nm, the material will turn into amorphous alloy. This method can be applied at room temperature, but cannot be used to fabricate big bulk amorphous materials.

Presently, liquid quenching is the most general process applied in fabricating amorphous alloys. It includes splat quenching, planar flow casting, roller quenching, spray forming, and so on. Liquid quenching can produce amorphous powders, foils, ribbons, bulk rods, and plates.

1-2   Evolution of thin film metallic glasses (TFMGs)

There are many methods to fabricate amorphous alloys, and most of them can form the large size of bulk metallic glasses. Bulk metallic glasses (BMG) are difficult to act as fine engineering materials because of their near-zero tensile ductility [6]. Owing to the high strength and hardness, amorphous alloys are also widely used as coating materials, as thin film metallic glasses (TFMGs). Until now, many techniques such as thermal evaporation and magnetron sputtering have been developed to prepare TFMGs.

The potential processes for fabricate of TFMGs were published since early 1980s. Schwarz and Johnson [1] first fabricated the La-Au TFMG by the solid-state reaction in 1983. They found the broad hump by X-ray diffraction (XRD) with Cu-K$_\alpha$ radiation, symbolizing the formation of amorphous structure. In 1986, Cotts et al. [2] successfully fabricated the

Ni-Zr multilayer thin films by sputtering, and observed the amorphization of crystalline metallic thin film by differential scanning calorimetry (DSC). Chen et al. [3] rapidly fabricated the amorphous Al-Fe, Bi-Fe and Bi-Ti alloys via co-sputtering in 1988. The thin film was deposited on the NaCl substrate cooled by liquid nitrogen. In late 1980s, Inoue's group [4] in Tohoku University of Japan developed many new multi-component bulk metallic glass systems with ower cooling rates such as the Mg-, Ln-, Zr-, Fe-, Pd-, Cu-, Ti- and Ni-based systems. Amorphous alloys started to be popularly noted and studied due to the overcome of the critical problem in fabrication.

In 1996, Dudonis et al. [5] produced the amorphous Zr-Cu TFMGs by co-sputtering. They first discussed the structure by change deposition factors, such as the working pressure and the substrate temperature. Besides sputtering, TFMGs can be fabricated by other deposition processes, such as pulse laser deposition. Comparing the sputter deposition and pulse laser deposition, the major difference is the kinetic energy of the incident atoms. The greater kinetic energy of the incident atoms would cause the formation of the metastable amorphous phase.

In near 2000, the Akira's group [6, 7] at Precision and Intelligence Laboratory developed the Zr-Cu-Al and Pd-Cu-Si ternary TFMGs, by alloy sputtering, for Micro Electro

Mechanical Systems (MEMS) applications. The benefit of alloy sputtering is that the deviation of composition between target and as-deposited films can be neglected. Moreover, because of a large super-cooled region, excellent three-dimension forming ability, good corrosion resistance and mechanical properties, the Zr- and Pd-based TFMGs are appropriate choices for the conical spring linear micro-actuator in MEMS. This report opened the TFMGs application in the MEMS industry.

Annealing-induced full amorphization in multi-component monolayer thin films was reported by Chu et al. [8] in 2004. The Zr-Al-Cu-Ni crystalline thin film was annealed under argon atmosphere at the heating rate of 40 K/min and the holding time of 60 s at the temperatures range from 550 to 950 K. The crystalline phase transferred to the metastable amorphous phase is due to the atomic inter-diffusion. Compared with direct fabrication methods of TFMGs, this method can save much energy and cost because it does not need to maintain the very low temperature of the substrate. Thus, the post-treatment methods are potential to fabricate TFMGs with the convenience and low cost.

In 2005, Inoue's group [9] fabricated the nano-device by the nano-scale pattering technique. The Zr-Al-Cu-Ni TFMGs were deposited by magnetron sputtering. The nano-pattern on the Zr-based TFMGs was produced by the focus ion beam (FIB) technology.

This nano-pattering technology may be applied to fabrication of nano-mold and high-density memories.

The evolution and improvement of TFMGs fabrication have been investigated by many researchers since 1960s. Several important characteristics of TFMGs, such as the electric resistance [10], hardness [11], fracture phenomena [12], reliability [13] and mechanical properties [6, 14], were studied. In 2005, Zhang et al. [15] reported the deformation behavior of free-standing Pd-based TFMGs. Upon bending, the as-deposited films revealed ductility due to the existence of shear bands. After annealing, the TFMGs become brittle because of the absence of shear bands.

Although bulk metallic glasses (BMGs) have been widely studied and used, little is known about applications of amorphous thin films for MEMS. Compared with conventional MEMS materials, TFMGs have the some advantages: (1) TFMGs are soft and show viscous flow in the supercooled liquid region, which makes them easy to be formed into a 3D shape. (2) In consequence of their mechanical isotropy, structural homogeneity, and absence of crystalline defects ,grain boundaries, segregation, etc., TFMGs are assumed to have no size effect; (3) TFMGs are a kind of amorphous alloys in which their physical properties can be adjusted by changing their compositions and contents as well as by precipitation of

nano-scaled particles.

1-3   Characteristics of Ta and its biomedical application

Tantalum is a gray, heavy, and very hard metal. And it is almost completely immune to chemical attack at temperatures below 423 K, and is attacked only by hydrofluoric acid, the acidic solutions containing fluoride ion, and free sulfur trioxide. Tantalum has a high melting point of 3290 K (boiling point of 5731 K), and is exceeded only by tungsten, rhenium and osmium. Tantalum is used to make a variety of alloys with desirable properties such as high melting point, high strength, and good ductility.

Tantalum (Ta) exists in two crystalline phases, alpha (α) and beta (β). The α-phase is relatively ductile and soft, it has body-centered cubic structure. The β-phase is hard and brittle, its crystal symmetry is tetragonal and electrical resistivity is relatively high. The β-phase is metastable and could convert to the alpha phase upon heating to 1023–1048 K. Bulk tantalum is almost entirely α-phase, and the β-phase usually exists as thin films prepared by magnetron sputtering, chemical vapor deposition or electrochemical deposition from an eutectic molten salt solution.

Ta-based alloys have been recently used in bioimplant, and have given remarkably effect. The metal tantalum has been the focus in orthopedics because of the stable biological character, good compatibility and typical structural nature. Experiments show that when the phagocytes contacted tantalum dust for 1 hour, they still stay alive and show no cell degeneration. This indicates that tantalum has non-cytotoxicity and no toxic effects on the human body.

As mentioned above, the special characteristics of tantalum provide great potential to apply to orthopaedic trauma. It can be made as wires thinner than a human hair filament, and then the filament can be used as surgical sutures. Tantalum wires have good corrosion resistance, excellent biocompatibility, and are non-toxic to humans. There is no need to conduct re-operation to remove and the implant can be kept in the body for whole lifetime.

1-4   Sputter process

1-4-1   Introduction to sputtering

The sputter deposition is a physical fabrication process of thin films, utilizing the ion bombardment and momentum transfer. The energetic particles impact the surface or

near-surface atoms of a target with enough energy which can break bonds and dislodge atoms by the bias between the anode and cathode. During this process, the collision between incident particles and atoms of a target can be viewed as elastic collision because the loss of momentum transfer is nearly zero. Sputtering occurs whenever any particle strikes a surface with enough energy to dislodge an atom from surface. The sputter yield Y is just the ratio of the number of emitted particles per incident particle [22]: Y = (number of emitter particles/ number of incident particles).

Sputtering can occur for virtually all incident species, including atoms, ions, electrons, photons, and neutrons as well as molecules and molecule ions. Generally speaking, the plasma includes inert gas ions, such as Ar^+, Kr^+, or small molecule ions such as N^{2+}, O^{2+}, etc. Sputter yield is independent on the particle charge but is dependent on the physical momentum transfer and kinetic energy from the incident particles to surface atoms.

When energetic particles bombard on the target, many reactions occur between the ionized gas particles and target atoms near the surface, as shown in Figure 1-2 [23]. Most of the transferred energy (>95 %) appear as heat in the surface region and near-surface region. Some of the bombarding particles are reflected as high energy neutrals and some are implanted into the surface. When an atomic sized energetic particle impinges on a surface,

the particle bombardment effects can be classed as:

(1)   Prompt effects ($<10^{-12}$ s) – lattice collisions, physical sputtering, reflection from the surface.

(2)   Cooling effects ($>10^{-12}$ s to 10^{-10} s) – thermal spikes along collision cascades.

(3)   Delayed effects ($>10^{-10}$ s to years) – diffusion, strain-induced diffusion and segregation.

(4)   Persistent effects – gas incorporation compressive stress due to recoil implantation.

Incident particles, also called as plasma, are produced by glow discharge. In the ultra-high vacuum chamber, dilute gas such as argon is introduced into the chamber. Gas molecules can be ionized when the bias between cathode and anode is large enough. At this moment, argon atoms are divided into Ar^+ ions and electrons. Electrons produced at the initial of glow discharge are called primary electrons. However, plasma cannot exist stably due to the unstable primary electron source. Actually, the stable plasma is maintained by stable secondary electrons source which are produced near the target surface by the collision between the ions and target atoms.

At the beginning of the discharge, the primary electrons from the cathode are accelerated by the electric field near the cathode to the anode. These energetic electrons collide with the

gas molecules and generate positive ions before travelling to the anode. The positive ions bombard the cathode surface and result in the generation of secondary electrons from the cathode surface. The secondary electrons increase the ionization of the gas molecules and generate a self-sustained discharge [24]. The advantages for sputtering deposition are

(1) Excellent film uniformity, particularly over large areas,

(2) Easy control of surface smoothness and uniform of films

(3) Deposition of films with nearly bulk-like properties, which are predictable and stable,

(4) The sputtering deposition is essentially a kinetic process involving momentum exchange rather than a chemical and/or thermal process. Therefore, virtually any material can be introduced into a gas discharge or sputtered from solid.

(5) Good adhesion of films.

(6) Sputtering allows for the deposition of the films having the same composition as the target source.

1-4-2 Sputtering systems

According to types of power supply, the sputtering systems can be divided into four types: (1) direct current (DC) diode sputtering system, (2) radio frequency (RF) diode

sputtering system, (3) magnetron sputtering, and (4) reactive sputtering.

The DC diode sputtering system is the simplest type of sputtering. Figure 1-3 [25] shows a pair of planar electrodes in a vacuum chamber. One electrode is a cold cathode, and the other is an anode. Glow discharge can occur with enough bias voltage. The top plasma-facing surface of the cathode is covered with a target material and the reverse side is water-cooled. The substrates are placed on the anode. After the glow discharge starts, Ar ions in the glow discharge are accelerated at the cathode, falling and bombarding the target and resulting in the deposition of the film on the substrates. Near the cathode is a dark space or sheath in which may collect large amounts of primary and secondary electrons. The RF diode sputtering system is very similar to the DC sputtering system, but is different from power supply, as shown in Figure 1-4 [25]. The DC system is suitable for conductor targets, such as Fe, Cu, Zr, Ni, and Mg.

By substitution of an insulator target for a metal target in a DC diode sputtering system, the sputtering glow discharge cannot be sustained due to the build-up of a surface charge of positive ions on the front side of the insulator target. To solve this problem, the RF power supply is substituted for the DC power supply. For a small part of the RF cycle, the cathode and anode are electrically reversed. This can eliminate the build-up charge on an insulating

surface by providing equal number of ions, electrons, and so on. The RF power supply is operated at high frequency from about 60 MHz to 80 MHz. However, the most common frequency is 13.56 MHz and its multiples [22].

A second key advantage of the RF diode system is that the oscillation of field in the plasma (at the driving frequency) could result in additional electron motion with the plasma. This has been described in several ways, but the most interesting point is an analogy to the electron "surfing" on the electric field waves in the plasma. The end result of this enhanced electron movement is that the probability of an ionizing collision is increased for a given secondary electron, and this leads to an increase in the plasma density compared to DC diode. The density increase results in higher ion currents and a faster sputtering rate.

Although the DC and RF sputter deposition processes are convenient, high reliability and continuous process, a slow deposition rate and charging are still the major disadvantages of these processes. In 1935, Penning's study [24] first revealed the low pressure sputtering under a transverse magnetic field which was added on a DC glow discharge tube. A magnetron uses a static magnetic field configured at the cathode location, as shown in Figure 1-5 [25]. The magnetic field is located parallel to the cathode surface, as shown in Figure 1-6 [22]. Secondary electrons emitted from the cathode due to ion bombardment are constrained

13

by this magnetic field to move in a direction perpendicular to both the electric field (normal to the surface) and the magnetic field. Figure 1-7 [22] shows an E × B drift, which is based on the Hall Effect. This drift causes electrons to move parallel to the cathode surface in a direction 90 degree away from the magnetic field.

Based on these issues mentioned, an additional magnetic field added can prolong the electron retaining time in the plasma and improve the probability of collisions. This enhances the efficiency of the simple diode sputtering, and also makes diode sputtering configuration operating under higher currents and pressures.

In reactive sputtering, thin films of compounds are deposited on substrates by the sputtering deposition from metallic targets which react with reactive gas such as oxygen, nitrogen with inert gas (invariably Ar). The types of compounds synthesized by reactive sputtering are oxides, nitrides, carbides, sulfides, and are briefly listed below [26]:

(1) Oxides (oxygen) – Al_2O_3, In_2O_3, SnO_2, SiO_2, and Ta_2O_5,

(2) Nitrides (nitrogen, ammonia) – TaN, TiN, AlN, and Si_3N_4,

(3) Carbides (methane, acetylene, propane) – TiC, WC, and SiC,

(4) Sulfides (H_2S) – CdS, CuS, and ZnS,

(5) Oxycarbides and oxynitrides of Ti, Ta, Al, and Si.

1-5 Development of Ta- and Zr-rich TFMGs with immiscible tantalum

Due to the well-developed sputtering techniques, binary and ternary TFMGs can be fabricated conveniently. The composition of available TFMGs can be also adjusted by additional targets via co-sputtering processes. According to the uniquely mechanical and medical properties as mentioned above, tantalum was chosen for the applicable additive in the Zr-based TFMGs recently. However, it was difficult to avoid the precipitation of the immiscible elements during the synthesis of Zr-based TFMGs and tantalum. To overcome this restriction, one conception was applied for these materials. From 2005 to 2007, Ma [27], Park et al. [28], and Liu et al. [29] addressed that an over-saturated amount of the immiscible element could be added to into the amorphous-alloy matrix during the deposition processes. Then, to compare with the liquid-quenching process for amorphous alloy with bulk or ribbon type, the solubility of immiscible element and glass forming composition range by the deposition processing were improved to show better enhancement [27-29].

In 2010, a series of Zr-Cu-Ti TFMGs with high solubility of immiscible tantalum were successfully fabricated via the co-sputtering processes by Chou et al. [30]. In these TFMGs, the content of tantalum can reach ~75% without precipitation. As shown in Figures 1-8(a)-(f),

these plane-view TEM bright-field images represent the uniform contract in the Zr-Cu-Ti-Ta TFMGs with the Ta content from ~12 to ~75 at%. No obvious nanocrystalline particles can be detected in these specimens. These results imply that the as-deposited Zr-Cu-Ti TFMG composed of the Zr-Cu-Ti amorphous solid solution with supersaturated immiscible Ta. When the addition of immiscible Ta is greater than 75 at%, nanocrystalline Ta starts to dominate the microstructure, as shown in Figures 1-8(g) and (h). In 2011, Chou et al. [31] further examined the microstructure of the Zr-Cu-Ti TFMGs with Ta content from 13 to 74 at%, as show in Figures 1-9(a)-(f), respectively. In the figures, the white contrast is caused by the presence of excessive Ta which has a higher Z number. The contrast becomes blurry when Ta is over 45at% and completely disappears at about 74 at%, shown in Figure 1-9(f). The structures of Zr-Cu-Ti-Ta films become nanocrystalline when Ta > 82%, including Ta82, Ta92, and pure Ta.

Moreover, the nanomechanical properties of Zr-Cu-Ti-Ta TFMGs were analyzed and performed by using a nanoindentation system [30]. The elastic moduli of the $Zr_{55}Cu_{31}Ti_{14}$ and β-Ta films were measured for the comparison; the values are 103 and 221 GPa, respectively. If the solubility of immiscible Ta is zero, meaning immiscible Ta would precipitate completely in the Zr-Cu-Ti TFMGs forming a composite, the resulting elastic modulus and hardness can be estimated via rule of mixture, either the Voigt or the Reuss model as the

16

upper or lower bound [32]. These calculated data can be compared with the experimentally

nanoindentation results and plotted in Figures 1-10(a) and (b). In the Figure 1-10(a), it shows

the variation of elastic modulus as a function of Ta content, in which the data can be divided

into region I (ZrCuTi-rich TFMGs), region II (Ta-rich TFMGs), and region III

(nanocrystalline β-Ta). It is obvious that the elastic moduli of specimens increase with Ta

content increasing from 50 to 75 at% in the region II. A transition point from region I to II at

Ta content of 50 at% implies that a drastic variation in atomic packing start to affect the

Zr-Cu-Ti-Ta TFMGs structure [30]. Furthermore, the variation of hardness to Ta content also

performs a similar trend, as shown in Figure 1-10(b). With increasing Ta content, the

measured hardness increases. For the maximum hardness in regions I and II of such TFMGs,

the enhancement of hardness is about 100% with respect to the hardness without the addition

of immiscible Ta. The hardness levels of the ZrCuTi-rich and Ta-rich TFMGs reach ~7 and

~10 GPa, respectively. As Ta is precipitated out in region III, the hardness increases rapidly to

a level ~20 GPa. In Figures 1-10(a) and (b), the experimental results are in poor agreement

with the calculated boundary values for the region II. The key is considered to be the

formation of Ta-Ta bonding. Ta serves as the major element in the amorphous structure,

indicating the self type of Ta-Ta bonds would form with a high population. Thus a higher

elastic modulus in region II would be achieved [30]. Consequently, in the Ta-rich

Zr-Cu-Ti-Ta TFMGs (with the Ta content of 50 to 75 at%), the mechanical properties can be

17

predominated by tantalum because of its superior properties and uniform distribution.

1-6   Metallic glass powders

1-6-1   Metallic glass powders fabrication

These BMGs powders can be fabricated by suction and injection casting. When the ingots were melted homogeneously by arc melting, the melt was immediately sucked into a water-cooled copper mold that has internal cylindrical-shaped cavities to fabricate the Zr- and Pd-based alloy rods under a purified argon atmosphere. The various copper molds with the cylindrical-shaped cavities inside could be replaced to prepare the cylindrical alloy rods with various sample sizes in diameter.

The injection casting can fabricate the master bulk metallic glass rods of Mg-Cu-Gd-Ag. First, the Mg-Cu-Gd-Ag master alloys fabricated by arc casting are taken appropriate amount and placed in a quartz tube, and the quartz tube needs to be sprayed a thin layer of boron nitride to avoid the interaction between alloy and quartz tube at high temperatures. The quartz tube is placed in an induction furnace controlled by the high frequency system, and the argon atmosphere is added to 1 atm in order to suppress the

generation of magnesium vapor. Similar to the arc melting process, the gas pouring and

flushing step is performed several times to ensure the high vacuum before injection casting.

The BMGs of Zr-Cu-Ni-Al and Mg-Cu-Gd-Ag can be fabricated by above processes.

And then milling these BMGs can gain the BMGs powders for this study.

1-6-2　Glass transition and crystallization temperatures

When the glasses are heated over glass transition temperature (T_g), they changed into

the supercooled liquid state. The supercooled liquid crystallizes when the temperature

exceeds crystallization temperature (T_x), and a metallic glass becomes a solid of the crystal

phase. The phase transition at T_g is reversible and that at T_x is irreversible.

1-7　Corrosion

1-7-1　Introduction

Corrosion can be defined as the phenomenon of material degradation caused by

chemical erosion which is reacted with external environment. Naturally the metallic minerals

are stable compounds, and most of the stable compounds are of the form of oxidation state. Therefore, as long as the conditions are sufficient in external environment, the metal will be transformed into the initial state (oxidation state), and this is the corrosion reaction.

Corrosion is an electrochemical reaction and it can be classified into eight categories [33] as shows in Figure 1-11.

(1) Uniform corrosion: Metallic surface generates a layer of uniform corrosion, meaning that the entire surface of the metal is doing the electrochemical reaction at the same time.

(2) Galvanic corrosion: This is also known as heterogeneous metal corrosion. When two different metals contact, the metal whose activity is larger would accelerate the corrosion reaction.

(3) Crevice corrosion: This means that the local electrochemical corrosion occurred in the gap and the stagnant solution which has covered on the surface. Because the dissolved oxygen in the aperture is more rarefied than the external, this area acts as the formation of anode, and the external oxygen-rich area is the cathode. The different concentration of oxygen in internal and external aperture forms oxygen concentration cell, and it results in the corrosion.

(4) Pitting corrosion: This only occurs in a metal material which has the passive film, and it is a partial erosion of the metal surface. The pitting corrosion can easily occur in the place which has impurities on the surface, non-uniform structure, and the uneven composition.

(5) Intergranular corrosion: The grain boundary has a strong chemical activity, so it may be more prone to corrosion at the position. When the alloy composition or impurities in the grain boundary separates, the grain boundary would generate potential difference and proceed corrosion reaction in the metal contact phase which has more negative potential. This corrosion would take place along the grain interfaces, causing the crack-like corrosion reaction.

(6) Selective corrosion: A particular metal is within a solid metal alloy because of the priority remove in this corrosion process. Usually the ingredients with active chemical characteristics would be extracted first.

(7) Erosion leaching: The corrosive fluid and the metal surface relative motion can cause the accelerated rate of metal corrosion. The feature is that the metal surface will have a groove hole and the direction is the same as the corrosive fluid flow direction.

(8) Stress corrosion: When the stress and corrosion exist at the same time, the metal will be gradually broken earlier before it reaches the breaking point. Stress corrosion

cracking (SCC) of metals is the breakdown of the metal surface that combines tensile stress and corrosive environment effects. During the SCC reaction, the material usually shows minor erosion, but the local crack spreads very quickly along the cross-sectional area in the metal. And the last causes serious damage.

1-7-2   The corrosion behavior of Zr and Ta

The corrosion behavior of Zr and Ta has been investigated by many companies. As show in Figure 1-11, this diagram [34] indicates the relationship between temperature and acid (H_2SO_4) concentration. If one needs to do a selective corrosion between Ta and Zr, the 80 wt% H_2SO_4 at 323 K could be a feasible way to try.

1-8   Dealloying

Dealloying is a corrosion process that can dissolve most electrochemically active part in an alloy system. This technique is widely used to fabricate crystalline material for nanoscale porosities as shown in Figure 1-12 [35]. There are some important parameters of dealloying process: the alloy composition, the electrode, and the electrochemical potential [36]. Furthermore, the initiation sites of the dealloying process are located on the defects, such as

grain boundaries and segregations. Recently, because of the investigation of two-phase amorphous alloys, the dealloying technique is possible for the metallic glasses. Additionally, it is always difficult to determine which phase is dissolved under dealloying process. Fortunately, the above difficulty can be overcome and clearly explained by Jayaraj et al. [36]. In their case, the XRD data showed that $Y_{20}Ti_{36}Al_{24}Co_{20}$ alloy exists two amorphous humps (Figure 1-13 [37]), they are Y-rich and Ti- rich phase, respectively. Hence, the 7 mm wide and 40 μm thick alloys of $Y_{56}Al_{24}Co_{20}$, $Ti_{56}Al_{24}Co_{20}$ and $Y_{20}Ti_{36}Al_{24}Co_{20}$ are selectively dealloyed by chemical and electrochemical treatment in a 0.1 M HNO_3 solution [36]. In Figure 1-14 [36], I-V curve showed that the Y-rich phase is more active in dissolution behavior than the Ti-rich phase. Moreover, the little difference of Ec between $Ti_{56}Al_{24}Co_{20}$ and $Y_{20}Ti_{36}Al_{24}Co_{20}$ indicates that the Y-rich phase of the two-phase amorphous alloy can be stripped out from the alloy without affecting the Ti-rich phase. Furthermore, the dealloying process can be regarded as a galvanic corrosion and $Y_{56}Al_{24}Co_{20}$ is more active in dissolution behavior than $Ti_{56}Al_{24}Co_{20}$. Hence, this suggests that the Y-rich phase would act as an anode while the Ti-rich phase would act as a cathode leading to a galvanic corrosion [36].

The ribbon specimens subjected to dealloying process were examined using a high resolution scanning electron microscope (SEM) with an energy dispersive X-ray spectrometer (EDS) and a transmission electron microscope (TEM). From the SEM image of porous

amorphous alloys formed by chemical and electrochemical dealloying, the nanosacle porosities are observed, as shown in Figures 1-15 (a) ~ (d) [36]. The EDS analysis showed that compositions of porous amorphous alloys are $Y_{5.4}Ti_{56.2}Al_{18.2}Co_{20.2}$ and $Y_{4.2}Ti_{56.5}Al_{11.2}Co_{28.1}$. These results clearly demonstrated that the porous morphology, as shown in Figure 1-15 [36] resulted from the dealloying of the Y-rich amorphous phase, containing high concentrations of Y and Al. TEM images of the $Y_{20}Ti_{36}Al_{24}Co_{20}$ alloy before and after dealloying are shown in Figures 1-16 (a) and (c) [36], respectively. According to the difference of TEM contrast and electron diffraction pattern (EDP), they clearly demonstrates that the Y-rich phase has been selectively dissolved, leaving the Ti-rich phase.

The dealloying technique is a good way to fabricate nanoporous metallic glasses. However, the electrochemistry I-V curve must be used to determine the proper pH condition for dealloying process and distinguish which phase is easy to dissolve.

1-9   Motivation

Metals are the oldest materials for biomedical implant and metallic alloys remain the good choice for applications involving hard tissue replacement. Porous BMGs has been studied as a kind of biomedical implant materials. It combines the advantages of metallic

24

foams and metallic glasses. Metallic foam materials exhibit properties like high compressive plastic strain and high energy absorption capacity, whereas metallic glasses have distinctive characteristics like high strength, wear resistance, and low processing temperature.

Pore forming techniques have been used for metallic glasses in liquid state and super-cooled liquid state as tools for foaming with the aid of some pore-formers like gas-generating flux additives, soluble place holders, and hollow carbon spheres. Since these external phases used for the foaming process would interact with the base alloy melting and reducing the glass forming ability, these techniques are limited to high glass forming groups like Pd-based and Zr-based alloys. Amorphous powders are easier to fabricate than bulk because of its high cooling rate in process. If there are different kinds of amorphous powders combining together and keeping in the metallic glasses form, the dealloying method can be applied to etch more active powders and fabricate metallic glass foams without the limit of high glass forming.

Until now, most of the bio-implant material is using the pure Ti or Ti-6Al-4V. The tissue in-growth properties of tantalum is better than titanium [38], so using the sputtering process to fabricate Ta-rich TFMGs on bio-implant material and etch the surface to make it rough or even porous can be of great beneficial in biomedical implant.

To sum up, in this study the dealloying corrosion method will be adopted to fabricate bulk metallic glass foams (BMGFs) with sizable porosity as well as the Ta-rich TFMGs with rough or even porous surface for bio-implant bone-nail materials.

Chapter 2 Experimental Procedures

In this study, the characterization after the dealloying corrosion processes of TFMGs and BMGs will be discussed. The flow chart of experimental procedures is shown in Figure 2-1. In this chart, tough TFMGs are fabricated via sputtering processes, and the BMGs fabrication are using thermomechanical analyzer (TMA) to give the bulk high temperature and pressure as sintering two different kind of amorphous powders. Doing the selective corrosion, in TFMGs, it should have phase separated and one of the separation phases is more active. In the BMGs, the more active amorphous metal is introduced as the glue in sintering. By this way, the selective corrosion might cause a porous or a rough-surface structure in TFMGs and BMGs.

2-1 Materials

For TFMGs, the Zr, Cu, Ti, and Ta metallic targets used in this study were purchased from Well Being Enterprise Co., Ltd, Taipei, Taiwan. The purity levels of the Zr, Cu, Ti, and Ta targets are 99.9%, 99.999%, 99.99%, and 99.9%, respectively. To simplify the deposition variation, the Zr-Cu-Ti alloy target, where the composition is $Zr_{65}Cu_{25}Ti_{10}$ in weight percentage (wt%), is used in multi-component co-sputtering. The purity of the Zr-Cu-Ti alloy

target is 99.9%. The pure Ti sheet which provided from Well-Being Enterprise Company with the size as 0.5 x 5 x 10 mm is used as the thin film substrate.

For fabricating BMGFs, there are three kinds of amorphous metallic powders and the compositions of each powder are $Mg_{58}Cu_{28.5}Gd_{11}Ag_{2.5}$, $Zr_{53}Cu_{30}Ni_9Al_8$, and $Ti_{40}Cu_{36}Pd_{14}Zr_{10}$. These powders are fabricated by the group of Professor J. S. C. Jang in National Central University. All of these three kinds of powders are measured about 30-50 μm.

2-2 Sample preparation

2-2-1 Film preparation

The Zr-Cu-Ti amorphous films can be fabricated using the co-sputtering deposition process with zirconium, copper, and titanium targets. A rotary pump was used to achieve mediate vacuum, and a cryo-pump was used to achieve a base pressure less than 1 x 10^{-6} torr. The base pressure maintains below 5 x 10^{-7} torr. There was a load-lock chamber, for quick and convenient exchanging of substrates without venting the main chamber. After achieving the base pressure, Ar was introduced into the chamber, and targets were pre-sputtered by inserting a movable shutter for five minutes. The films were fabricated by the co-sputtering

with the $Zr_{65}Cu_{25}Ti_{10}$ (wt%) alloy target and the pure Ta target, which were both set on the DC cathodes. The purity of $Zr_{65}Cu_{25}Ti_{10}$ and Ta target is 99.9% and 99.95%, respectively. Before processing, the base pressure of the chamber is at 5 x 10^{-7} torr or greater. The Zr-Cu-Ti-Ta films were fabricated at a fixed power of 300 W for the Zr-Cu-Ti cathode and power of 300 W for the Ta cathode. The thickness of all as-deposited Zr-Cu-Ti-Ta alloy thin films lies within 2~3 µm.

2-2-2   Sintering

The TMA was applied in the sintering process. The $Mg_{58}Cu_{28.5}Gd_{11}Ag_{2.5}$ and $Zr_{53}Cu_{30}Ni_9Al_8$ amorphous powders were sintered at the supercooled liquid region of $Mg_{58}Cu_{28.5}Gd_{11}Ag_{2.5}$ and the temperature between the liquid temperature (T_l) of $Mg_{58}Cu_{28.5}Gd_{11}Ag_{2.5}$ and the T_g of $Zr_{53}Cu_{30}Ni_9Al_8$, respectively. The process was carried out from room temperature to sintering temperature at a heating rate of 10^oC/min and holding at sintering temperature for 50 minutes. Furthermore, in order to enhance the combination of the powders, a load about 5 N was applied during sintering process.

The other instruments are Instron University Testing Machine 5582 (Figure 2-2) and high temperature furnace. Instron 5582 offered high pressure to combine these metal powders,

and the high temperature furnace (Figure 2-3) could control the temperature during the

pressing process. There are two combinations of powders such as $Mg_{58}Cu_{28.5}Gd_{11}Ag_{2.5}$ mixed

in $Zr_{53}Cu_{30}Ni_9Al_8$ powders and $Zr_{53}Cu_{30}Ni_9Al_8$ mixed in $Ti_{40}Cu_{36}Pd_{14}Zr_{10}$ powders. The

sintering temperature for the $Mg_{58}Cu_{28.5}Gd_{11}Ag_{2.5}$ mixed in $Zr_{53}Cu_{30}Ni_9Al_8$ powders is $150^{o}C$,

and sintering temperature for the $Ti_{40}Cu_{36}Pd_{14}Zr_{10}$ powders mixed in $Zr_{53}Cu_{30}Ni_9Al_8$ powders

is $410^{o}C$. Both cases adopted the sintering time of 10 min, in avoiding the possible

crystallization effect. Also, after sintering pressing for 10 min, the powder materials did not

seem to undergo any flowing or deformation.

2-3   Property measurements and analyses

2-3-1   X-ray diffraction (XRD)

The nature of the thin film fabricated by the magnetic sputtering deposition is examined

by X-ray diffraction (XRD). The SIEMENS D5000 X-ray diffractometer with

CuK_{α} radiation ($\lambda = 1.5406$ Å), operated at 40 kV and 30 mA, and equipped with 0.02 mm

graphite monochromer, is utilized.

2-3-2   Differential scanning calorimetry (DSC)

By using differential scanning temperature as shown in Figure 2-4 (power compensation, Figure 2-5), the glasses forming ability parameters such as T_g, T_x, T_m, and T_l can be detected. In this study, the thermal behavior of the $Mg_{58}Cu_{28.5}Gd_{11}Ag_{2.5}$ and $Zr_{53}Cu_{30}Ni_9Al_8$ amorphous powders was measured under the constant heating rate of $0.33^oC/s$ and the heating range from 50-327^oC for the Mg based MG powders, from 50-727^oC for the Zr and Ti based MG powders, by using the Perkin Elmer Pyris differential scanning calorimeter. Therefore, T_g, T_x, T_m and T_l of Zr, Mg and Ti powders were quantified, and these parameters could provide the basis for the sintering process.

2-3-3　Optical microscopy (OM)

The optical microscopy is used to examine the basic morphology of the samples at lower magnifications. There are eyepiece with 10X and objective lens with 2X, 10X, 20X and 50X. The roughness and amount of scratches were surveyed. The dirt and oxide could also be founded by OM and weeded out before the further analysis.

2-3-4　Scanning electron microscopy (SEM) and energy dispersive spectrometry (EDS)

The microstructure of the surface of the samples was observed by the JEOL JSM 6400 SEM. The morphology of the BMGs was observed by secondary electron image (SEI), and the distribution of the powders in BMGs could be perceived by backscatter electron image (BEI). The composition of these powders after doing the heat treatment was examined by energy dispersive X-ray spectrometry (EDS).

2-3-5   Compression testing

Room temperature compression test were performed on the cylindrical glassy rods by a Instron 5582 universal testing machine. According to the stress-strain curve, the compressive strength, observed elastic modulus and plastic strain can be determined. Before starting compression testing, the specimen was cut from the cylindrical glassy rod with the high-to-diameter ratio (h/d) of ~2, providing a normal aspect ratio of 2:1, as recommended by ASTM E9-89a (2000) for testing high strength materials. To accurately measure the change of sample displacement during deformation, the Instron 5582 universal testing machine was assembled with the Instron 2601 Linear Variable Differential Transformer (LVDT) displacement transducer.

In the preparation of test samples, the samples were first sliced from the as-cast

cylindrical rods using a Buehler diamond cutter. The two ends and cylindrical surfaces of cut

samples were ground by silicon carbide abrasive papers with water and polished completely.

A custom sample jig was used to carefully grind and polish the top and bottom cross-section

surfaces not only to ensure parallelism between two ends of cut sample, but also to confirm

that the two ends are exactly perpendicular to the longitudinal axis of sample. The perfect

geometry of sample should be ideally perpendicular alignment between the compression

surface and cylindrical axis. If the test sample is ground and polished by hand, it is likely to

produce a slight misalignment between the compression surfaces and cylindrical axis, for

example, some samples produced by this way showed tilts of ~1° or slightly more, which is a

geometrical. Each sample was carefully centered on the loading axis to ensure the uniaxial

loading. The applied strain can be calculated according to the crosshead displacement after

correction for machine compliance. Multiple compression tests were performed for

confirming the reliability of mechanical properties.

2-3-6 Electrochemical analysis

The electrochemical behavior of the amorphous Zr-, Ti- and Mg-based alloys are studied

by potentiodynamic polarization and linear sweep voltammetry measurements which are

conducted by CHI 614D (Figure 2-6) electrochemical work station in a three electrodes cell

(Figure 2-7). The counter and reference electrode are platinum wire and Ag/AgCl, and specimens are used as a working electrode. Before potentiodynamic polarization measurements, the specimens are allowed to stabilize in HNO_3 until the open-circuit potential (OCP) changed by no more than 0.4 mV/5 min. The potential chemical reactions between the MGs and acid solution are characterized using a linear sweep voltammetry with the scanning potential from 0 V to 3 V with a scan rate 0.01 V/s. In addition, the anodic polarization scan is started from -0.5 V to 0.5 V with a scan rate 0.5 mV/s. The corrosion current density (I_{corr}), corrosion potential (E_{corr}) and corrosion rate can be determined by the Tafel extrapolation method from the anodic polarization curves.

2-3-7 Porosity measurement

Porosity is a static property – it can be measured in the absence of flow.

$$\text{Porosity} = \varphi = \frac{V_p}{V_b} = \frac{V_b - V_m}{V_b} \; , \tag{2.1}$$

where ϕ = porosity, V_p = pore volume, V_m = matrix volume, and V_b = bulk volume of reservoir sample = $V_m + V_p$. The porosity of the sintered specimens after the etching or dealloying process can be measured by the Archimedes method.

$$V_p = \frac{W_{sat} - W_{dry}}{\rho_{fluid}}, \tag{2.2}$$

$$V_m = \frac{W_{dry} - W_{sub}}{\rho_{fluid}}, \tag{2.3}$$

34

$$V_b = \frac{W_{sat} - W_{sub}}{\rho_{fluid}}. \qquad (2.4)$$

By inserting equations (2.2), (2.3) and (2.4) into equation (2.1):

$$\varphi = \frac{W_{sat} - W_{dry}}{W_{sat} - W_{sub}}, \qquad (2.5)$$

In equations (2.2)-(2.5), W_{sat} is weight of the sample with fluid in its pores, W_{dry} is weight of the sample, and W_{sub} is weight of the sample in fluid.

Chapter 3 Results and Discussion

3-1 Sample preparation

3-1-1 Thin film metallic glasses (TFMGs)

Zr-Cu-Ti-Ta thin film metallic glasses (TFMGs) can be fabricated by co-sputtering. Considering the limit of the sputtering instrument and the simplification of the fabrication process, it is easier to control the composition via the co-deposition of Zr-Cu-Ti and Ta cathodes. The Zr-Cu-Ti TFMGs with various amounts of tantalum addition were fabricated by this procedure. The Zr-Cu-Ti-Ta TFMGs were processed at the constant value (300 W) of the Zr-Cu-Ti and Ta cathodes. In this condition, the composition of thin film is $Ta_{57}Zr_{23}Cu_{12}Ti_8$. The Ta content in the ZrCuTi-rich film would increase with increasing Ta cathode power, as shown in Figure 3-1 [31].

3-1-2 Bulk metallic glass foams (BMGFs)

As show in Table 3-1, the basic thermal properties of the resulting ribbons were obtained by DSC. These data can be used as the basis of subsequent sintering process to bind

the powders.

The DSC scan results for the three MG powders, the $Zr_{53}Cu_{30}Ni_9Al_8$, $Ti_{40}Cu_{36}Pd_{14}Zr_{10}$, and $Mg_{58}Cu_{28.5}Gd_{11}Ag_{2.5}$ powders are presented in Figures 3-2 (a) to (c) [42-44], and list in Table 3-1 for the T_g, T_x, and ΔT_g. Note that Tg for the three MG powders are 425, 147, and 396°C, respectively.

To prepare the Zr- and Mg-based BMGFs, the $Mg_{58}Cu_{28.5}Gd_{11}Ag_{2.5}$ powders, used as spacer, were mixed with the $Zr_{53}Cu_{30}Ni_9Al_8$ powders. These two powders were blended in acetone to insure sound mixture. Then, the mixture was pressed as slugs at a pressure of 10 MPa by Press Ingot Device instrument. The structure shown in Figure 3-3 is the OM picture before sintering heat treatment. It can be observed that this slug has a loose structure.

For the sintering heat treatment, the temperature was firstly selected to be 180°C which is about 30°C above the T_g temperature of the Mg-based BMG powders. The pressure was set to be about 5 N by TMA to test whether the viscous Mg based metallic glassy powders can be combined or glued as filling the pores between the Zr-based powders. The structure after sintering at 180°C was found to be poorly bound. The OM picture shown in Figure 3-4 indicates that the Mg- and Zr-based powders in this structure were closely packed, but the Zr

powders mostly kept separated, as indicated for the region of the Mg- and Zr-based BMGs in

Figure 3-4. If this structure is subjected to corrosion experiment, it should be collapsed. Thus,

the sintering temperature was raised to $395^{o}C$, over the T_m temperature of the Mg-based

BMG powders and approaching the T_g temperature of the Zr-based BMG powders. The

purpose of raising the sintering temperature is to force the Zr-based BMG powders to be

bonded together and closely. After sintering at this temperature, the Zr-based powders can

now be combined together and show the porous structure, as exhibited in Figure 3-5.

Since that the sintering heat treatment above conducted in TMA could not offer enough

pressures to well combine these powders, another method using the Instron universal testing

machine 5582 equipped with a high temperature furnace was then adopted. By this new

method, the pressure can be adjusted depending on the cross-sectional area of the sintering

holder. Instron 5582 can only provide a maximum load of 10,000 N on our holder with a

diameter of 6 mm, and therefore 350 MPa was the limit of this pressing system. The

three-zone high temperature furnace can control the sintering temperature in highly accurate

degrees. The Zr- and Mg-based powders were then sintered at 350 MPa and $150^{o}C$, about the

T_g of Mg based MG powders, and the combination was found to be quite satisfactory.

Another BMGF combination is the $Zr_{53}Cu_{30}Ni_9Al_8$ and Ti-based powders, sintering at

410$^\text{o}$C with the compression pressure of 350 MPa. The T_g and T_x temperatures are 425 and

500$^\text{o}$C for the Zr based MG powders and 396 and 447$^\text{o}$C for the Ti based MG powders. The

Zr-based MG powders overlap their supercooled region with the Ti-based MG powders from

425 to 447$^\text{o}$C. But the pressure might reduce the T_g slightly, and the materials could start

flowing at 410$^\text{o}$C.

3-2 Electrochemical tests

The Zr-, Ti- and Mg-based BMGFs are selectively dealloyed by electrochemical

treatments in 0.1 M HNO$_3$ (pH = 1) solution. For the electrochemical treatment, the Zr-, Ti-

and Mg-based BMGFs are immersed in the 0.1 M HNO$_3$ solution. The process of dealloying

is carried out in a corrosion cell with the glassy alloy as working electrode, and platinum and

Ag/AgCl as counter and reference electrodes, respectively. In order to make certain of the

electrochemically dealloying reaction on the entire specimen, a potential above the dealloying

threshold, or the critical potential (E_c), was applied for a predetermined period time about 5

hours. The E_c for various alloy systems, as mentioned above, can be determined by the

method of the anodic polarization. The anodic polarization curve can clearly demonstrate the

distinct chemical behavior of the alloys.

For the $Zr_{53}Cu_{30}Ni_9Al_8$ ribbon, which was immersed in 0.1 M HNO_3, the critical potential E_c in anodic polarization curve is about 2.17 V (Figure 3-6), the corrosion current, I_{corr}, is 3.35 x 10^{-6} A/cm^2 and the corrosion potential, E_{corr}, is -0.45 V, as shown in Figure 3-7. In Figures 3-8 and 3-9, the $Ti_{40}Cu_{36}Pd_{14}Zr_{10}$ powders, when immersed in 0.1 M HNO_3, E_c is about 2.30 V, the I_{corr} is 1.85 x 10^{-6} A/cm^2 and the E_{corr} is -0.27 V. Because the BMGFs are combined together by two kinds of powders, they can be treated as a two-phase amorphous alloy. The values of I_{corr} and E_{corr} demonstrate that the $Zr_{53}Cu_{30}Ni_9Al_8$ phase is more reactive than the $Ti_{40}Cu_{36}Pd_{14}Zr_{10}$ phase, and the value of E_c that $Ti_{40}Cu_{36}Pd_{14}Zr_{10}$ need a higher voltage than $Zr_{53}Cu_{30}Ni_9Al_8$ to make the chemical reaction to occur. This difference in the dissolution potentials of the alloys indicates that within a potential range from 2.17 V to 2.30 V, the $Zr_{53}Cu_{30}Ni_9Al_8$ phase of the two-phase amorphous alloy can be removed from the alloy without affecting the $Ti_{40}Cu_{36}Pd_{14}Zr_{10}$ amorphous phase. In order to increase the reaction rate of the $Zr_{53}Cu_{30}Ni_9Al_8$ phase to the greatest extent, the potential was chosen to supply an E_c of 2.3 V that is already about the threshold E_c of the $Ti_{40}Cu_{36}Pd_{14}Zr_{10}$ amorphous phase. Figure 3-10 shows the variation of current density after the corrosion reaction, a roughness surface can be observed. This result demonstrated that the selective corrosion has happened, and the more details of surface morphology are shown by SEM observations in Sec. 3.4.

3-3 XRD analysis

The as-deposited $Ta_{57}Zr_{23}Cu_{12}Ti_8$ thin film on glass substrate presents a broad diffraction hump characteristic of amorphous nature without distinct crystalline peaks, as shown in Figure 3-11. The amorphous signal consists of a hump located at the diffraction angle range of 32° to 45°.

Figures 3-12 and 3-13 show the XRD patterns of the Zr- and Ti-based MG powders, the former has diffused peak position at 36.9^o and the latter at 41°. Figure 3-14 shows the XRD pattern of the mixed powders after sintering at 410^oC for 10 min of the Zr- and Ti-based MG powders, consisting of a broad diffraction peak characteristic of amorphous structure with no crystalline phases. The broad diffuse hump located at the diffraction angles of about 35° to 45°, and the peak position at 40°. There is only one diffused peak because of the overlapping of the amorphous XRD humps of the Zr- and Ti-based MG powders.

The sintered specimens were further immersed in solution for dealloying. The resulting etched rod that combined by the Zr- and Ti-based still shown amorphous diffuse peak and the peak position is about 41°, as shown in Figure 3-15. This means that the etching dealloying process did corrode the Zr-based MG powders, remaining the sintered Ti-based MG powders.

3-4　SEM SEI and BEI observations

3-4-1　Thin film metallic glasses (TFMGs)

The E_c of $Ta_{57}Zr_{23}Cu_{12}Ti_8$ thin film metallic glass is about 2.7 V in 0.1 M $H_2SO_{4(aq)}$, obtained by electrochemical test. Thus, the reaction is carried out at 3.0 V in 0.1 M $H_2SO_{4(aq)}$. Observation of the surface morphology is conducted by SEM to see whether it occurs nano-porous or not. The SEM images, shows in Figures 3-16 and 3-17, are the etched surface of the amorphous $Ta_{57}Zr_{23}Cu_{12}Ti_8$ TFMG. The thin film without etching at a magnification of 5000X, as shown in Figure 3-16, presents a smooth surface. Figure 3-17 shows the $Ta_{57}Zr_{23}Cu_{12}Ti_8$ etched thin film observed at two magnifications of 1000X and 5000X. Porous structure cannot be seen, but lots of small etched voids on the thin film surface. It seems that there is no obvious phase separation as the paper mentioned, the perfect nano-porous structure cannot be obtained.

3-4-2　Bulk metallic glass foams (BMGFs)

The sintered powder samples (without etching or dealloying) were firstly examined by

SEM/EDS at a low magnification. The well-bound Zr- and Ti-based MG powder specimens, as shown in Figure 3-18.

.

The distribution and the composition of powders were examined under the BEI mode, as one example shown in Figure 3-19. In the BEI image, the brighter domains, gray domains, and darker domains can be observed. The few dark domains are the pores and the surrounding regions are still intact, indicating that the structure is well combined and bound. At the 300X magnification, the EDS examinations identify the compositions in the brighter domains and the gray domains, as shown in Figures 3-20 and 3-21, respectively. These results disclose that the compositions of the brighter domains are the $Zr_{63.8}Ni_{16.2}Cu_{15}Al_5$ MG powders (the atomic number Z for Zr is 40, imposing higher Z-contrast), and the gray domains are the $Ti_{40}Cu_{36}Pd_{14}Zr_{10}$ amorphous powders (the atomic number Z for Ti is 22, resulting in lower Z-contrast).

After the etching dealloying process, immersed in the 0.1 M HNO_3 solution with 2.3 V for 5 hours, it remains only the sintered Ti based powders, with lots of pores on the surface that can be observed in the SEI and BEI micrographs. Figure 3-22 show the representative Zr- and Ti-based sintered specimens after the etching or dealloying process in HNO_3 for 5 hours. It is apparent that there are many pores in various sizes. The typical pore size is about

43

$10 \sim 30\ \mu m$.

The typical BEI image of the sintered and etched specimens is shown in Figure 3-23. The EDS examinations on these powders reveal that the powders are all Ti based MG powders. Figures 3-24 to 3-27, shows the SEM/BEI and EDS results taken from different positions with a magnification of 300X, and they showed the dominant phase is the $Ti_{40}Cu_{36}Pd_{14}Zr_{10}$ MG powders. But there are few places still with higher Zr contents, reflecting the minor retained Zr MG powders.

3-5 The porosity measurement

The weight of W_{sat}, W_{air} and W_{sub} were measured by electronic balance. The value of W_{sat} is 0.025 g, of W_{air} is 0.022 g, and of W_{sub} is 0.018 g. Based on Equations (2.1) – (2.5), the porosity can be calculated to be $\varphi = 0.43$, or the porosity is 43%.

3-6 Simulated body-fluid and electrochemical biocompatibility tests

In order to compare the bio-compatibility of some representative metallic glassy materials by simple in vitro tests, simulation body-fluid immersion is used to test the

corrosion resistance of some self-made metallic glasses, namely, $Mg_{65}Cu_{25}Gd_{10}$, $Mg_{67}Cu_{25}Y_8$, $Zr_{61}Cu_{17.5}Ni_{10}Al_{7.5}Si_4$ and $Fe_{70}B_{20}Si_{10}$. The biocompatibility of the current $Ti_{40}Cu_{36}Pd_{14}Zr_{10}$ BMGF has not been finished, but will be explored in the next stage. A novel electrochemical test by measuring the cyclic voltammetry response of the metallic glasses in the simulation body-fluid is developed. With this approach, analyzing the electrochemical response of the metallic glasses in body can be achieved in a short time.

The cyclic voltammetry testing results are shown in Figure 3-28. A standard pure Ti screw was also measured as the standard for this test. The result illustrates that the standard pure Ti remains no redox peak and the charge current induced by pure Ti is also small, while the $Fe_{70}B_{20}Si_{10}$ metallic glass exhibits strong redox reaction from 0 V to 1 V. Alternatively, the Zr-based metallic glassy alloy obviously has much lower current response. However, in comparison with the standard pure Ti, the current response of the Zr-based MG is still slightly higher at high potential levels. The inset in Figure 3-28 shows an enlarged CV curve for the Zr-based MG. Through comparison with the CV response curves obtained individually from pure elements of Zr, Cu, Ni, Al and Si, the redox hump, shown in the insert of Figure 3-28 for $Zr_{61}Cu_{17.5}Ni_{10}Al_{7.5}Si_4$, between -0.4 V and 0 V is expected to be caused by the very minor oxidation of Al or Cu in the Hank's solution. The Zr-based metallic glassy alloy shows the best potential for the further biocompatibility research in the human body. The

biocompatibility of the current $Ti_{40}Cu_{36}Pd_{14}Zr_{10}$ BMGF will be explored in the next stage.

Chapter 4 Conclusion

(1) There are two main reasons that the selective corrosion reaction of the $Ta_{57}Zr_{23}Cu_{12}Ti_8$ TFMGs does not occur. First, it does not show the obvious phase separation. The second one is the close chemical property of the α-phase and β-phase Tantalum. Once the corrosion reaction occurs, the entire $Ta_{57}Zr_{23}Cu_{12}Ti_8$ TFMG samples are etched simultaneously. No nano-scaled porous structure can be prepared by the dealloying process.

(2) A two-phase sintered specimen, combining two kinds of amorphous MG powders with different chemical activities, has been fabricated. The electrochemical test can present the corrosion condition for each phase easily. The corrosion current (I_{corr}) and corrosion potential (E_{corr}) of the amorphous MG powders or sintered mixed specimens can be determined by the electrochemical test.

(3) From observation of SEM SEI and BEI micrographs, the $Zr_{53}Cu_{30}Ni_9Al_8$ MG powders show more corrosion reactive than the $Ti_{40}Cu_{36}Pd_{14}Zr_{10}$ MG powders. The current dealloying process provides an easy way in preparing a porous network structure of metallic glasses without requiring a high glass forming ability.

(4) The current pore size in the porous structure of the $Ti_{40}Cu_{36}Pd_{14}Zr_{10}$ BMGFs is about 10 ~

30 μm, and the porosity volume ratio of about 43%. For bio-implant applications, the

pore size needs to be further increased to 200-500 μm. This can be achieved by using

much larger Ti and Zr based starting MG powders. Meanwhile, the porosity ratio should

be further increased to 60-80%. This can also be achieved by using more Zr based MG

powders, so that a great volume can be corroded away, reaching a much higher porosity

ratio.

(5) The biocompatibility of various metallic glasses under *in-vitro* tests shows that the

$Zr_{61}Cu_{17.5}Ni_{10}Al_{7.5}Si_4$ metallic glass exhibits the best corrosion resistance and none

short-term cytotoxicity. Although there is a small electrochemical response in the

simulation body-fluid of Hank's solution, this metallic glass still shows its potential for

biomedical application. The biocompatibility of the current $Ti_{40}Cu_{36}Pd_{14}Zr_{10}$ BMGF will

be explored in the next stage.

References

[1] W. L. Johnson. MRS Bull, **24**, 42-56 (1999).

[2] A. C. Lund and C. A. Schuh, Journal of Applied Physics, **95**, 4815-4822 (2004).

[3] M. P. Staiger, A. M. Pietak, J. Huadmai, and G. Dias, Magnesium and its alloys asorthopedic biomaterials: a review. Biomaterials, **27**, 1728-1734 (2006).

[4] H. S. Chou, J. C. Huang, T. H. Lai, L. W. Chang, X. H. Du, J. P. Chu and T. G. Nieh, J. Alloy Compd., **483**, 341-345 (2009).

[5] B. Golding, B. G. Bagley and F. S. L. Hsu, Phys. Rev. Lett., **29**, 68-70 (1972).

[6] Y. Wang, J. Li, A. V. Hamza and T. W. Barbee, Proc. Natl. Acad. Sci. U. S. A., **104**, 11155-11160 (2007).

[7] R. B. Schwarz and W.L. Johnson, Phys. Rev. Lett., **51**, 415-418 (1983).

[8] E. J. Cotts, W. J. Meng, and W. L. Johnson, Phys. Rev. Lett., **57**, 2295-2298 (1986).

[9] Q. M. Chen, Y. D. Fan, and H. D. Li, Mater. Lett., **6**, 311-315 (1988).

[10] A. Inoue, Acta Metar., **48**, 279-306 (2000).

[11] J. Dudonis, R. Brucas, and A. Miniotas, Thin Solid Films, **275**, 164-167(1996).

[12] S. Hata, K. Sato, and A. Shimokohbe, Proc. SPIE, **3892**, 97-108 (1999).

[13] Y. Liu, S. Hata, K. Wada, and A. Shimokohbe, Jpn. J. Appl. Phys., **40**, 5382-5388 (2001).

[14] J. P. Chu, C. T. Liu, T. Mahalingam, S. F. Wang, M. J. O'Keefe, B. Johnson, and C. H. Kuo, Phys. Rev. B, **69** 113410 (2004).

[15] P. Sharma, W. Zhang, K. Amiya, H. Kimura, and A. Inoue, Nanoscience and Nanotech., **5,** 416-420 (2005).

[16] J. Sakurai, S. Hata, and A. Shimokohbe, *International Conference on Advanced Technology in Experimental Mechanics 2003*, 10-12 (2003).

[17] G. P. Zhang, Y. Liu, W. Wang, and J. Tan, Appl. Phys. Lett., **88**, 013105 (2006).

[18] G. P. Zhang, Y. Liu, and B. Zhang, Scripta Mater., **54,** 897-901 (2006).

[19] R. Yamauchu, S. Hata, J. Sakurai, and A. Shimokohbe, Mater. Res. Soc, Symp. Proc., **894**, 0894-LL02-05.1-0894-LL02-05.5 (2006).

[20] S. Hata, T. Fukushige, and A. Shimokohbe, Proceedings of CPT2002, 162-167 (2002).

[21] G. P. Zhang, Y. Liu, and B. Zhang, Adv. Eng. Mater., **7**, 606-609 (2005).

[22] K. Seshan, *Handbook of Thin-Film Deposition Processes and Techniques*, Noyes Publications, Park Ridge, N.J., USA (1988).

[23] D. M. Mattox, *Handbook of Physical Vapor Deposition (PVD) Processing*, Noyes Publications, Westwood (1998).

[24] K. Wasa, and S. Hayakawa, *Handbook of Sputter Deposition Technology*, Noyes Publications, Park Ridge, NJ, (1991).

[25] W. Zou, *Synthesis of Giant Magnetoresistive Multilayers*, University of Virginia, (2001).

[26] M. Ohring, *The Material Science of Thin Films*, Academic Press, San Diego (1992).

[27] E. Ma, Prog. Mater. Sci., **50**, 413-509 (2005).

[28] E. S. Park, D. H. Kim, T. Ohkubo, and K. Hono, J. Non-cryst. Solids, **351,** 1232-1238 (2005).

[29] L. Liu, K. C. Chan, M. Sun, and Q. Chen, Mater. Sci. Eng. A, **445-446**, 697-706 (2007).

[30] H. S. Chou, J. C. Huang, L. W. Chang, Surface & Coatings Technology, **205**, 587-590 (2010).

[31] H. S. Chou, X. H. Du, J. C. Huang, and T. G. Nieh, Intermetallics, on line (2012).

[32] R. L. Zong, S. P. Wen, F. Zeng, Y. Gao, and F. Pan, J, Alloys Compd., **464**, 544-554 (2007).

[33] 柯賢文，腐蝕及其防制，全華科技圖書股份有限公司，2006 年.

[34] The Tantaline Company (http://www.tantaline.com/Sulfuric-Acid-Graphs-57.aspx).

[35] J. Erlebacher, M. J. Aziz, A. Karma, N. Dimitrov, K. Sieradzki, Nature, **410,** 450 (2001).

[36] J. Jayaraj, B. J. Park, H. Kim, W. T. Kim and E. Fleurya, Scripta Materialia, **55**, 1063 (2006).

[37] B. J. Park, H. J. Chang, D. H. Kim, W. T. Kim, Appl. Phys. Lett., **85,** 6353 (2004).

[38] Hironobu Matsuno, Atsuro Yokoyama, Fumio Watari, Motohiro Uo, Takao Kawasaki, Biomaterials, **22**, 1253-1262 (2005).

[39] H. M. Chen, Master Thesis, *Analysis of plasticity and shear band deformation mechanism in bulk metallic glasses and composites, National Sun Yat Sen University* (2009).

[40] T. A. Gruen, R. A. Poggie, D. G. Lewallen, Radiographic evaluation of a monoblock acetabular component. Arthroplasty, **3**, 369-378 (2005).

[41] A. C. Fischer-Crippers, Vacuum, **58**, 569-585 (2000).

[42] Jason S.C. Janga, S.R. Jian , C.F. Changa, L.J. Changa, Y.C. Huanga, T.H. Li , J.C. Huangb, C.T. Liuc, Journal of Alloys and Compounds, **478**, 215–219 (2009).

[43] Fengxiang Qin, Masahiro Yoshimura, Xinming Wang, Shengli Zhu1,Asahi Kawashima, Katsuhiko Asami and Akihisa Inoue, Materials Transactions, **48**, 1855–1858 (2007).

[44] S.-R. Jian, J.-B. Li, K.-W. Chen, Jason S.-C. Jang, J.-Y. Juang, P.-J. Wei, J.-F. Lin, Intermetallics, **18**, 1930–1935 (2010).

Table 3-1   Summary of thermal properties for the Zr-Cu-Ni-Al and Mg-Cu-Gd-Ag BMG

powders obtained from DSC.

BMG powders	T_g (^{o}C)	T_x (^{o}C)	ΔT_x (^{o}C)
$Zr_{53}Cu_{30}Ni_9Al_8$	425	500	75
$Mg_{65}Cu_{25}Gd_{10}$	147	207	60
$Ti_{40}Cu_{36}Pd_{14}Zr_{10}$	396	447	51
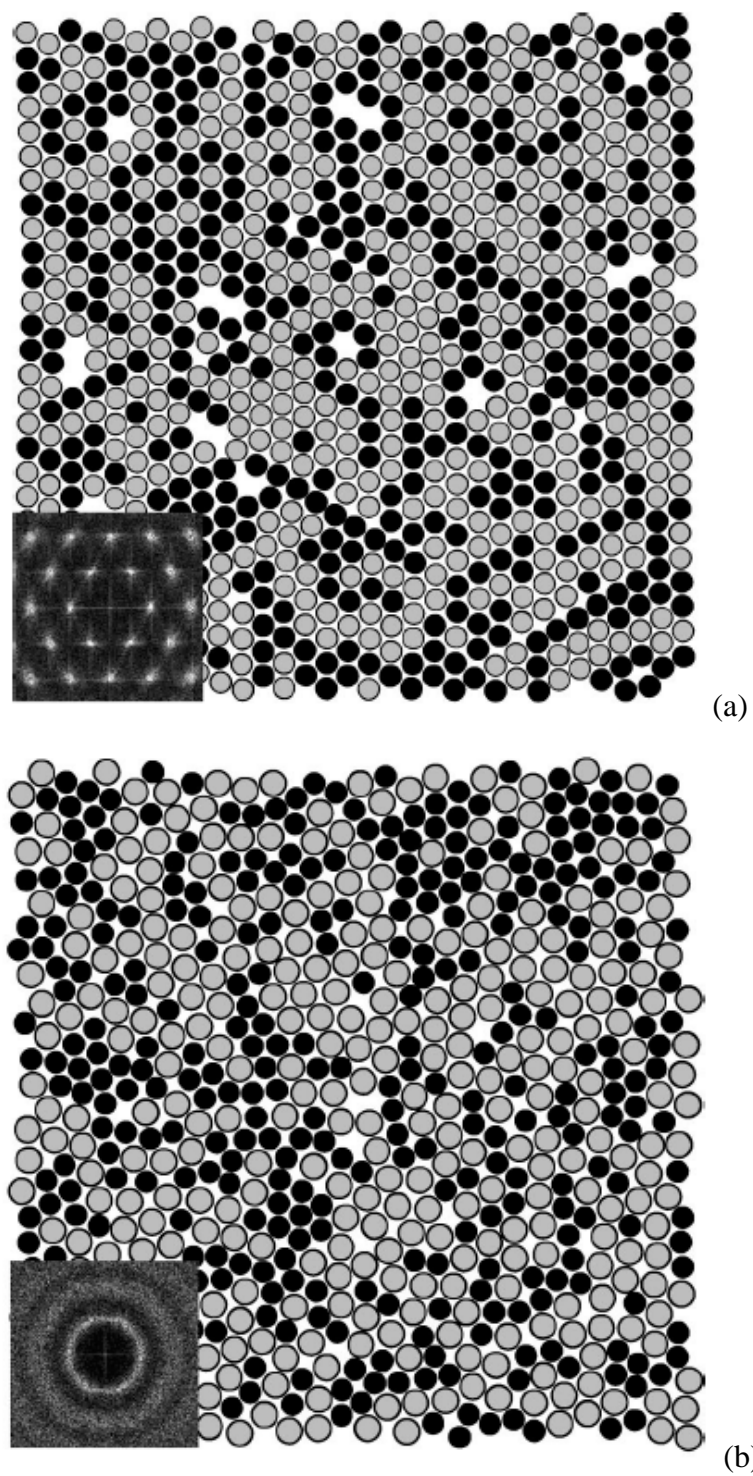
Figure 1-1   A scheme of (a) long-range-ordered structure and (b) short-range-ordered

structure.
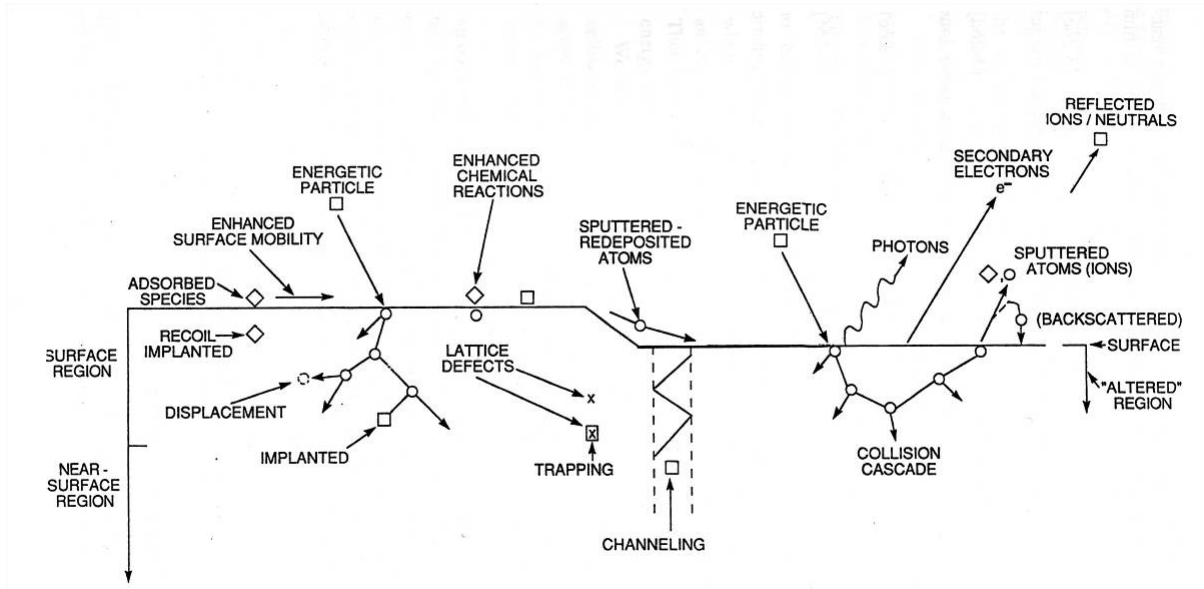
Figure 1-2   Events that occur on a surface being bombarded with energetic atomic-sized particles [23].
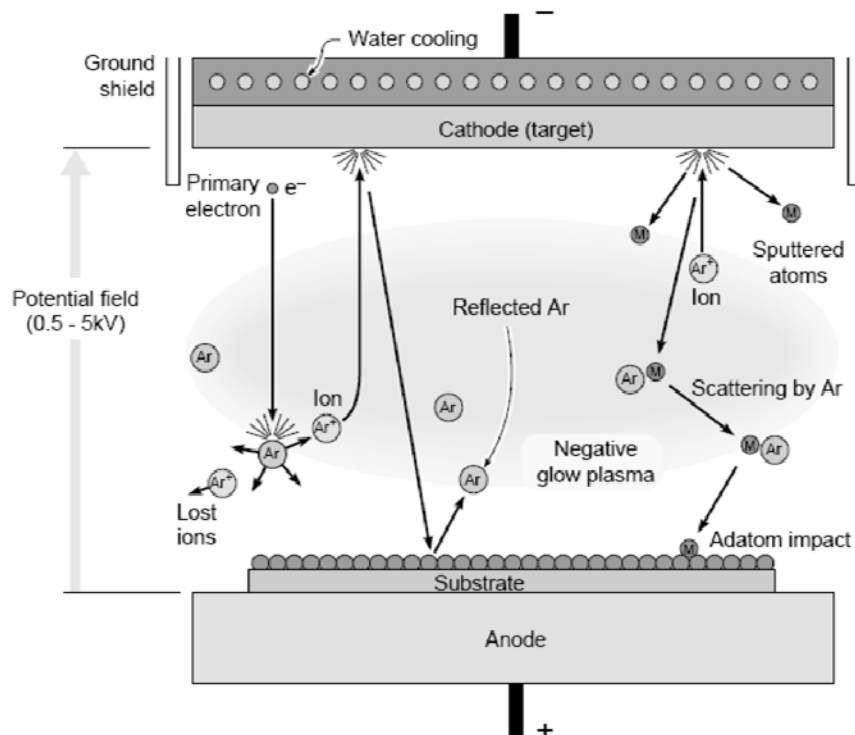
Figure 1-3   A schematic illustration of a DC diode Sputtering System [25].
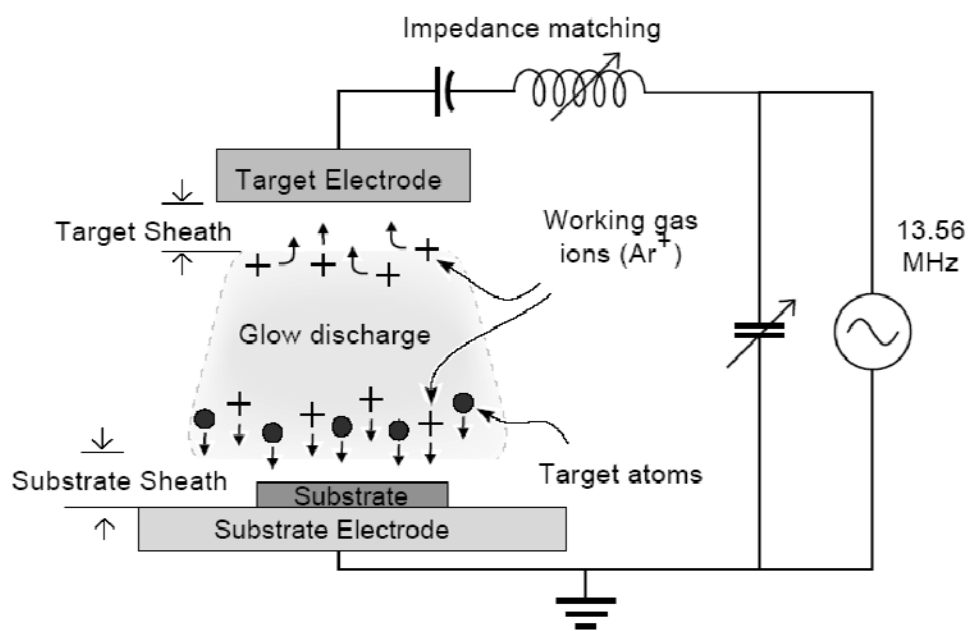
Figure 1-4   A schematic illustration of the RF diode sputtering deposition [25].
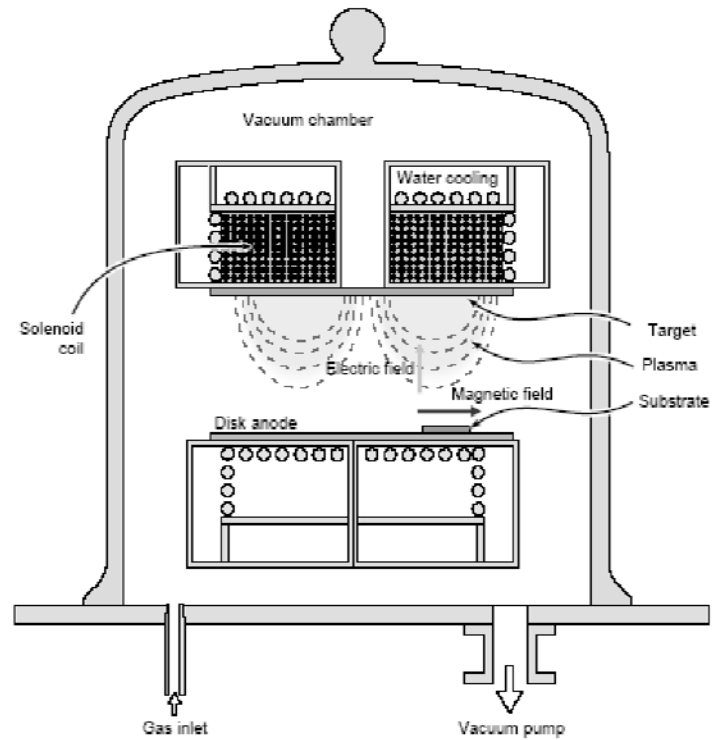
Figure 1-5   A schematic illusion of a planar magnetron sputtering system [25].
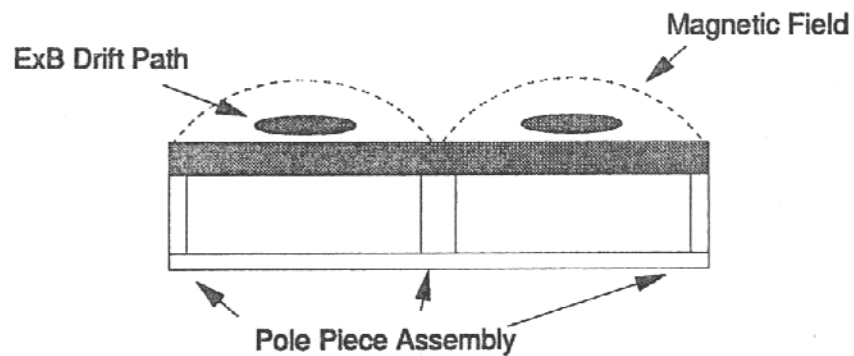
Figure 1-6   The side view of the magnetic field configuration for circular planar

magnetron cathode [22].

57
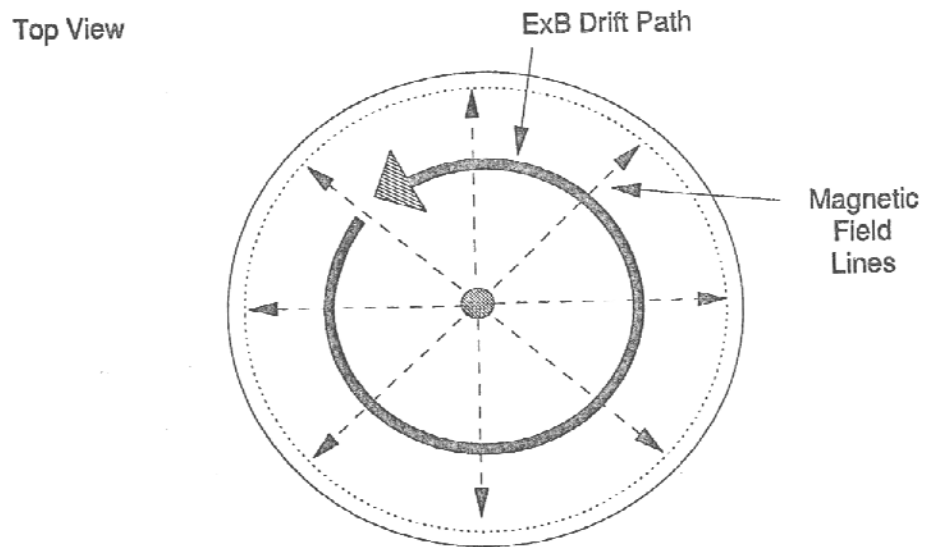
Figure 1-7   The top view of the magnetic field configuration for a circular planar

magnetron cathode [22].
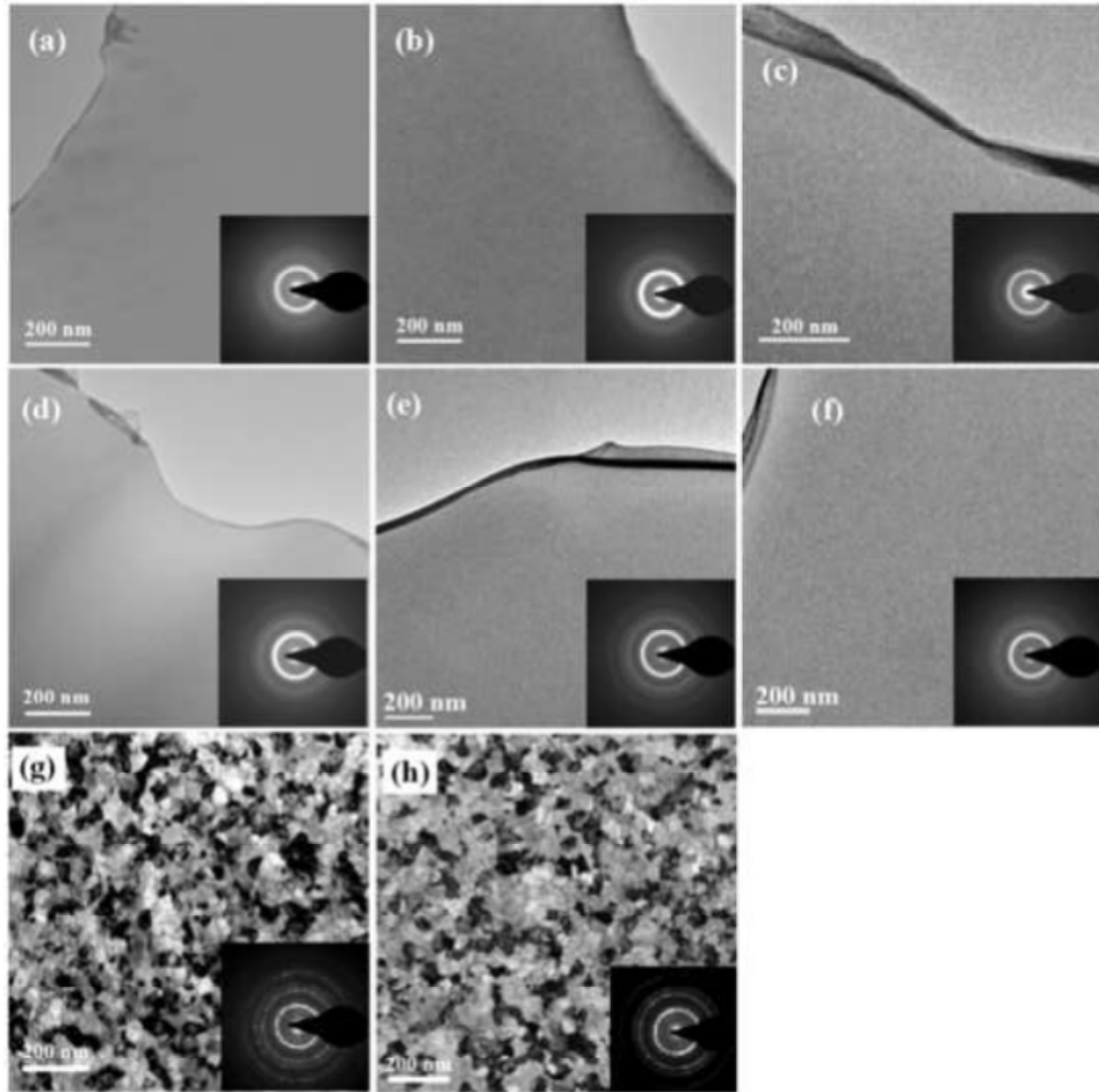
Figure 1-8 Bright-field TEM images of (a) $Zr_{45}Cu_{27}Ti_{15}Ta_{13}$, (b) $Zr_{41}Cu_{23}Ti_{12}Ta_{24}$, (c) $Zr_{31}Cu_{15}Ti_{10}Ta_{44}$, (d) $Zr_{23}Cu_{12}Ti_8Ta_{57}$, (e) $Zr_{19}Cu_6Ti_7Ta_{68}$, (f) $Zr_{14}Cu_7Ti_5Ta_{74}$, (g) $Zr_{10}Cu_5Ti_3Ta_{82}$, and (h) $Zr_4Cu_3Ti_1Ta_{92}$ (with inserted selected area diffraction patterns) [30].
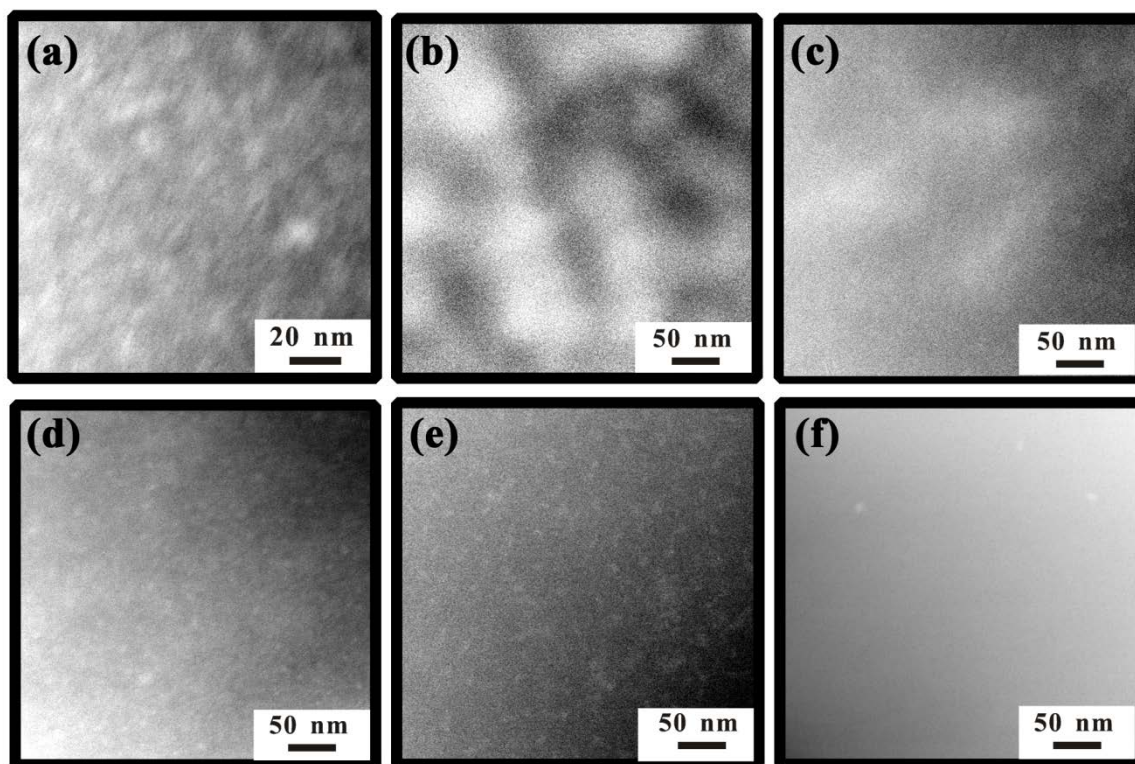
Figure 1-9   HAADF images of (a) Ta13, (b) Ta24, (c) Ta44, (d) Ta57, (e) Ta68, and (f)

Ta74. All samples exhibit two-phase structures except Ta74 which is a single

phase [31].
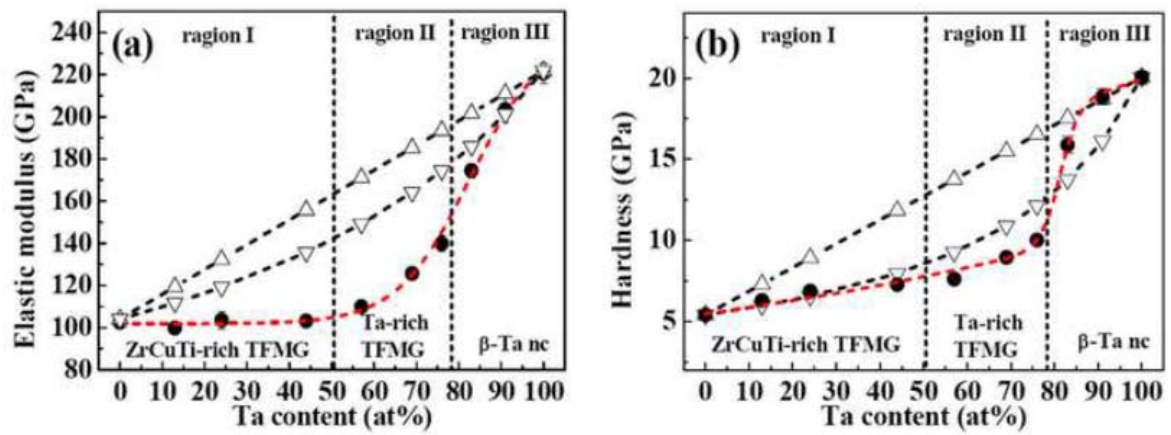
Figure 1-10 Relationship between (a) elastic modulus and (b) hardness of ZrCuTiTa TFMGs and Ta content. The upper bound (Δ) and the lower bound (∇) are calculated by the Voigt and Reuss models, respectively. The experimental value of elastic modulus and hardness (●) are measured by nanoindentation [30].
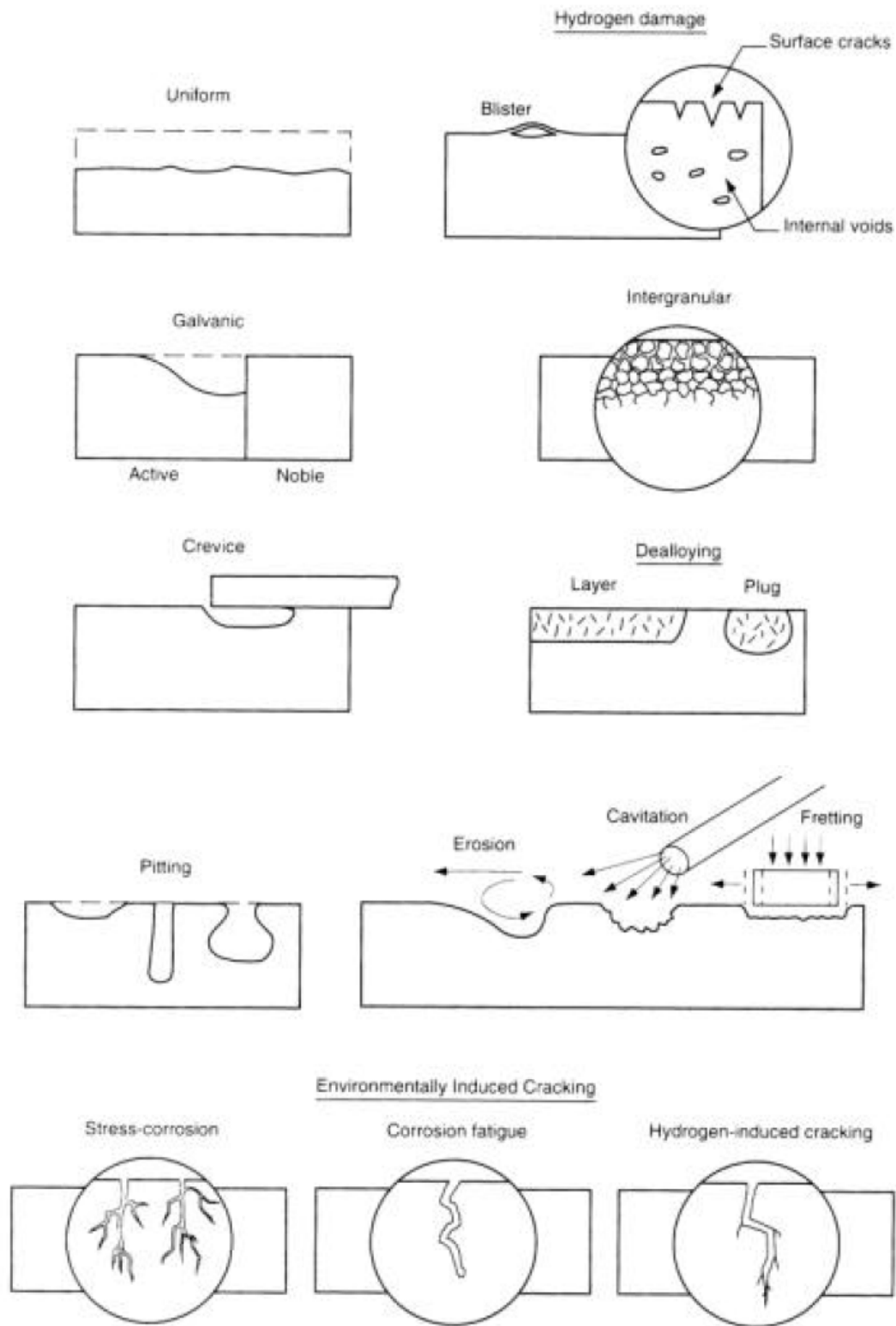
Figure 1-11 The various types of corrosion behaviors for metallic materials [33].
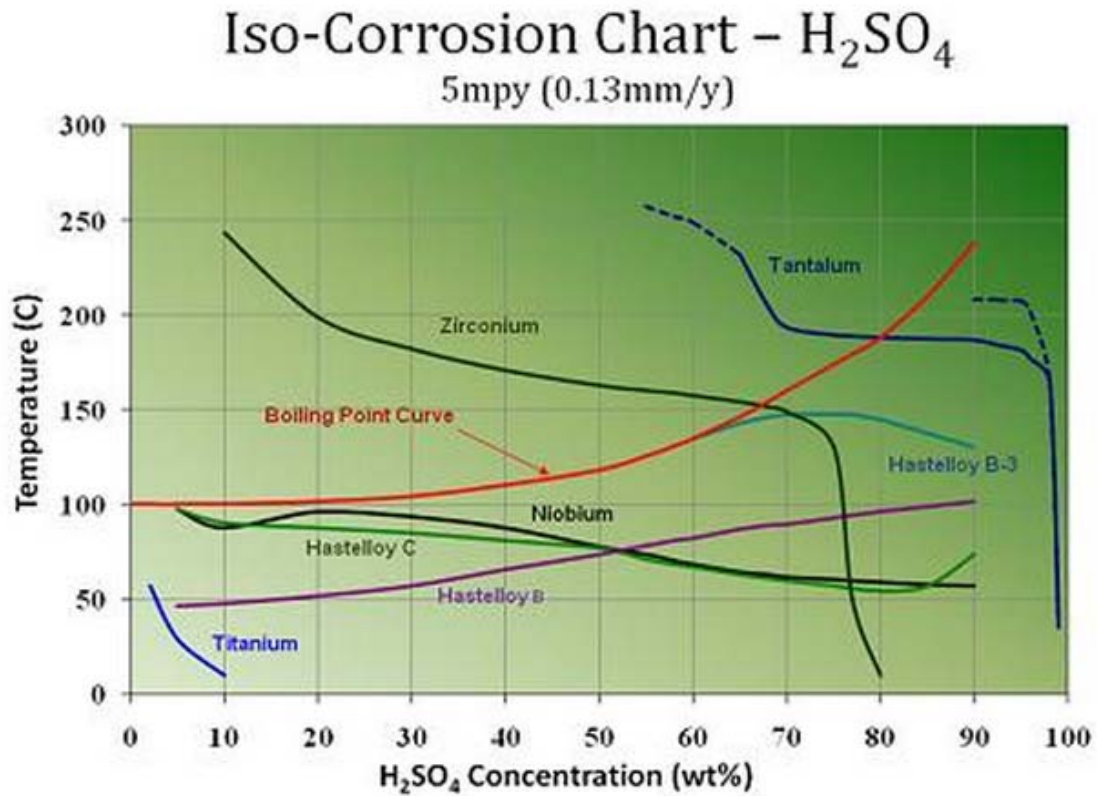
Figure 1-12   The sulfuric acid iso corrosion curves [34].
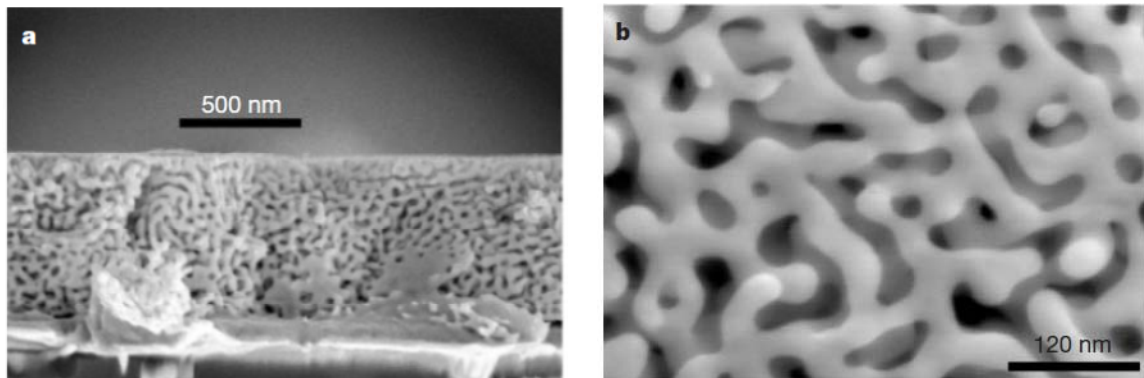
Figure 1-13   Scanning electron micrographs of nanoporous gold made by selective

dissolution of silver from Ag-Au alloys immersed in nitric acid under free

corrosionconditions. (a) Cross-section of dealloyed $Au_{32}Ag_{68}$ thin fillm. (b)

Plan view of dealloyed $Au_{26}Ag_{74}$ [35].
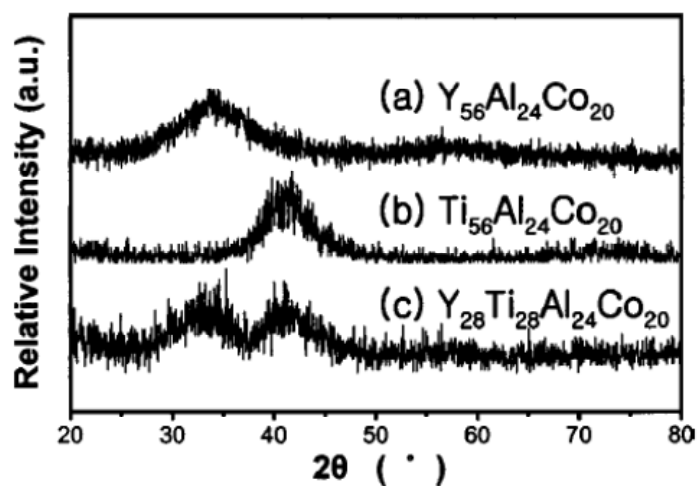
Figure 1-14   XRD   patterns   obtained   from   melting   spinning: (a) $Y_{56}Al_{24}Co_{20}$,   (b)

$Ti_{56}Al_{24}Co_{20}$, and (c) $Y_{28}Ti_{28}Al_{24}Co_{20}$ alloys [37].
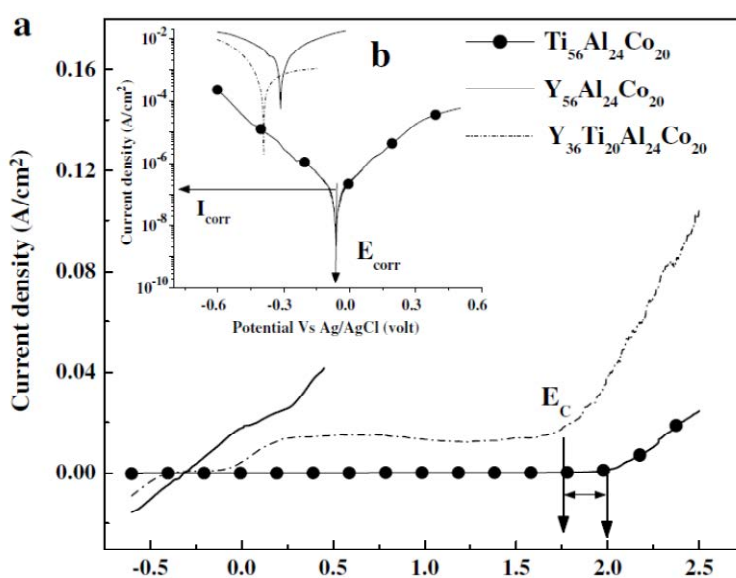
Figure 1-15   (a)   Anodic   polarization   behaviors   for   the $Y_{56}Al_{24}Co_{20}$, $Ti_{56}Al_{24}Co_{20}$

monolithic amorphous alloys and $Y_{20}Ti_{36}Al_{24}Co_{20}$ two phase amorphous alloy

in 0.1 M HNO_3 (pH = 1) solution. (b) Tafel slope analysis of the polarization

curves in Figure 1(a) [36].
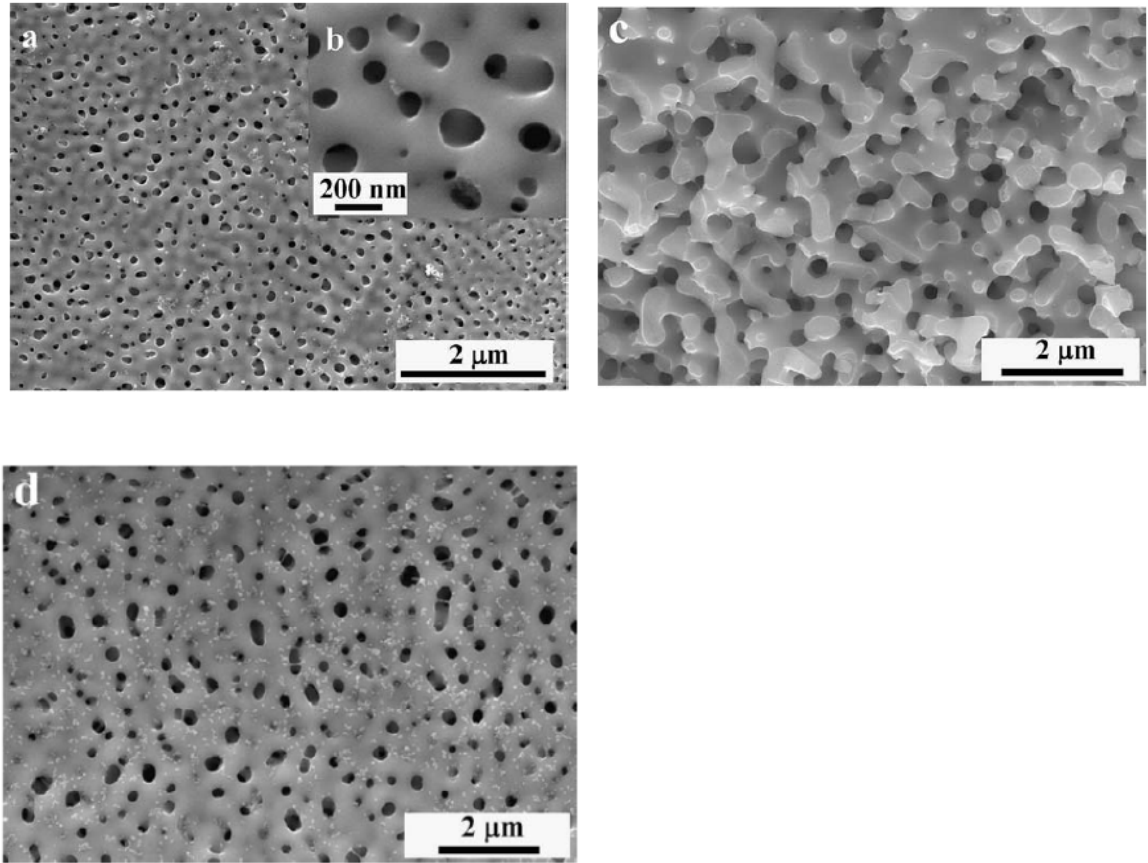
Figure 1-16 SEM images showing the formation of porous morphology of $Y_{20}Ti_{36}Al_{24}Co_{20}$

two-phase amorphous alloy. (a)–(c) Chemically dealloyed $Y_{20}Ti_{36}Al_{24}Co_{20}$

alloy in 0.1 M HNO3 solution for 24 h: (a) low magnification demonstrating

pore formation; (b) magnified image showing three-dimensionally connected

open type pores; (c) crosssection of the dealloyed ribbon specimen. (d)

Electrochemically dealloyed $Y_{20}Ti_{36}Al_{24}Co_{20}$ alloy in 0.1M HNO3 solution

with an applied voltage of 1.9 V for 30 min [36].
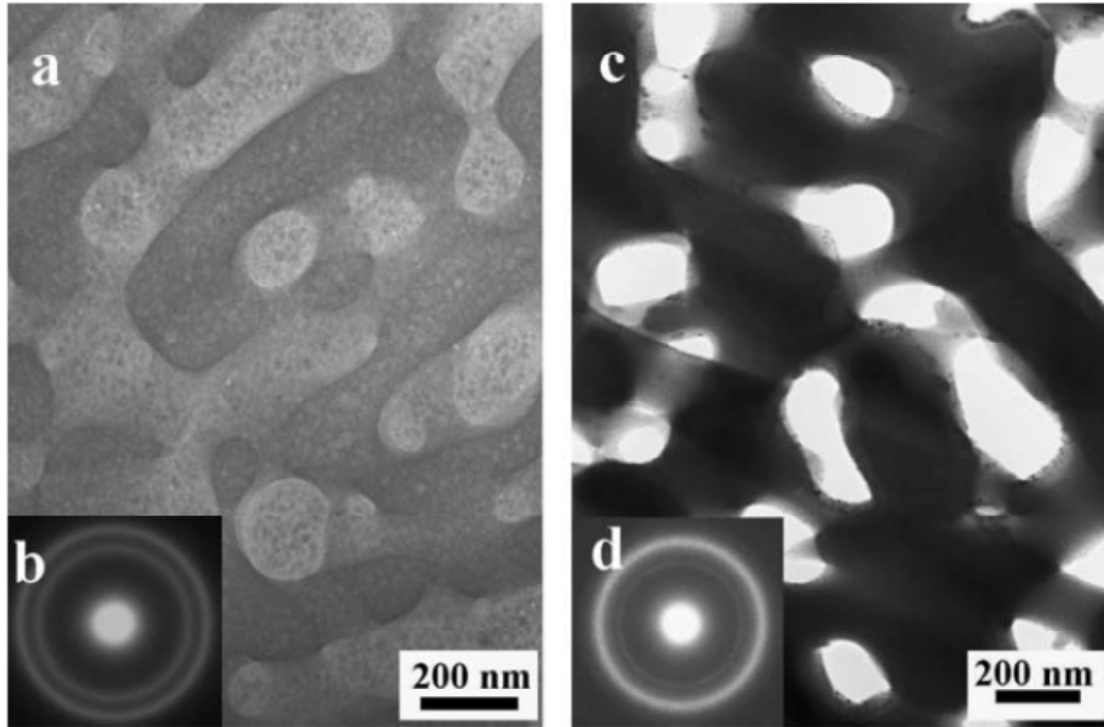
Figure 1-17 (a) TEM image of $Y_{20}Ti_{36}Al_{24}Co_{20}$ two-phase amorphous alloy before

dealloying process and (b) corresponding EDP; (c) TEM image

$Y_{20}Ti_{36}Al_{24}Co_{20}$ two-phase amorphous alloy after dealloying process and (d)

corresponding EDP [36].
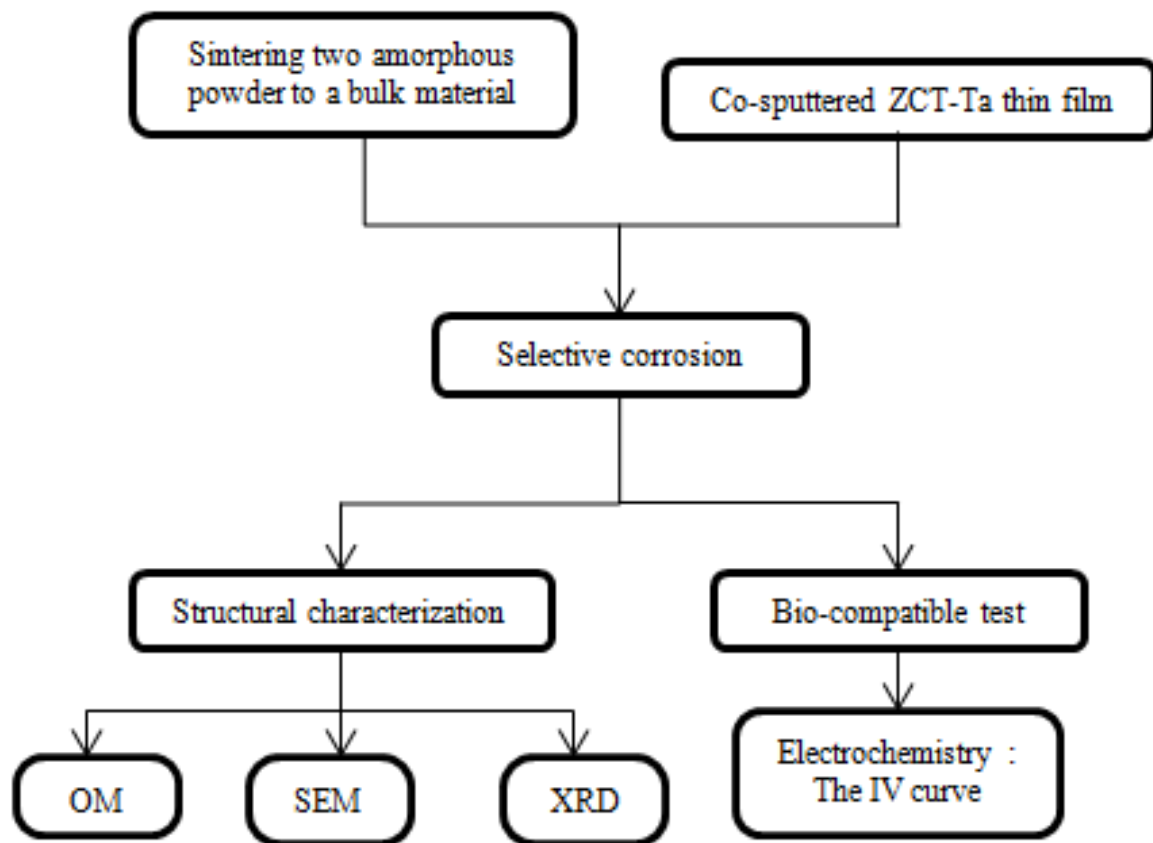
Figure 2-1   The flow chart of the experimental procedures in this study.

Figure 2-2   The picture of the Universal Testing Machine Instron 5582.

Figure 2-3   The picture of three-zone high temperature furnace attached to the Universal

Testing Machine Instron 5582.

Figure 2-4   The picture of Perkin Diamond Pyris DSC.
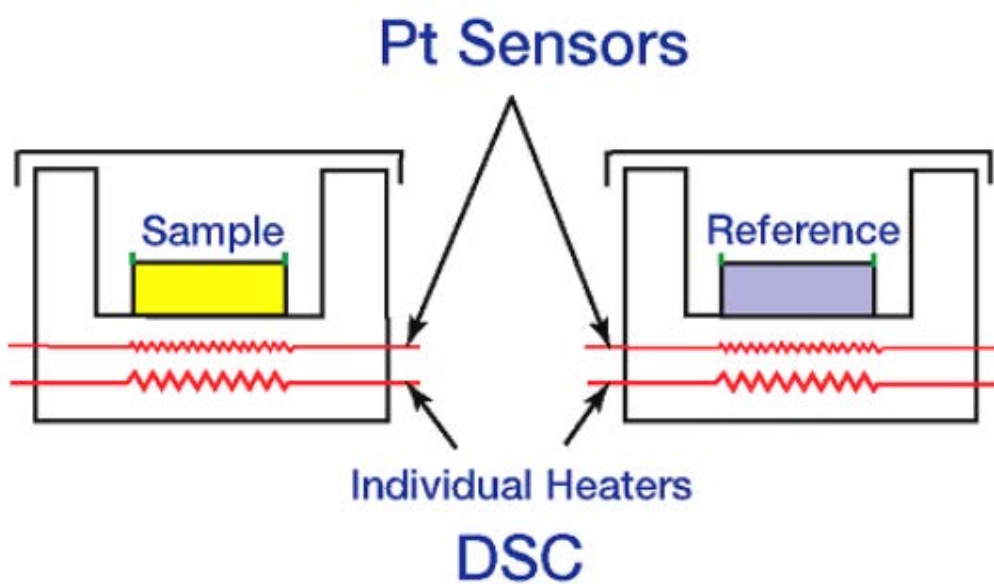
Figure 2-5   The schematic diagram of power compensation DSC.

Figure 2-6   The picture of CHI614D electrochemical work station.
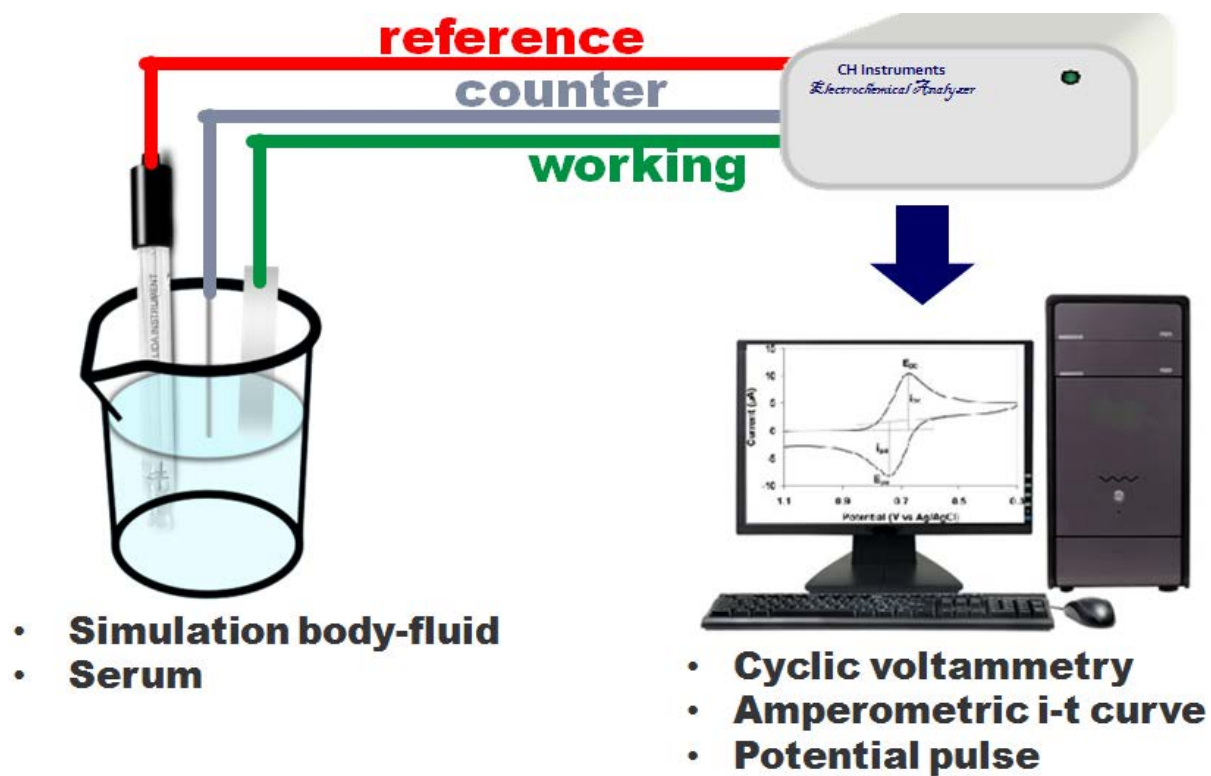
Figure 2-7   Schematic diagram of electrochemical workstation in a three electrodes cell.
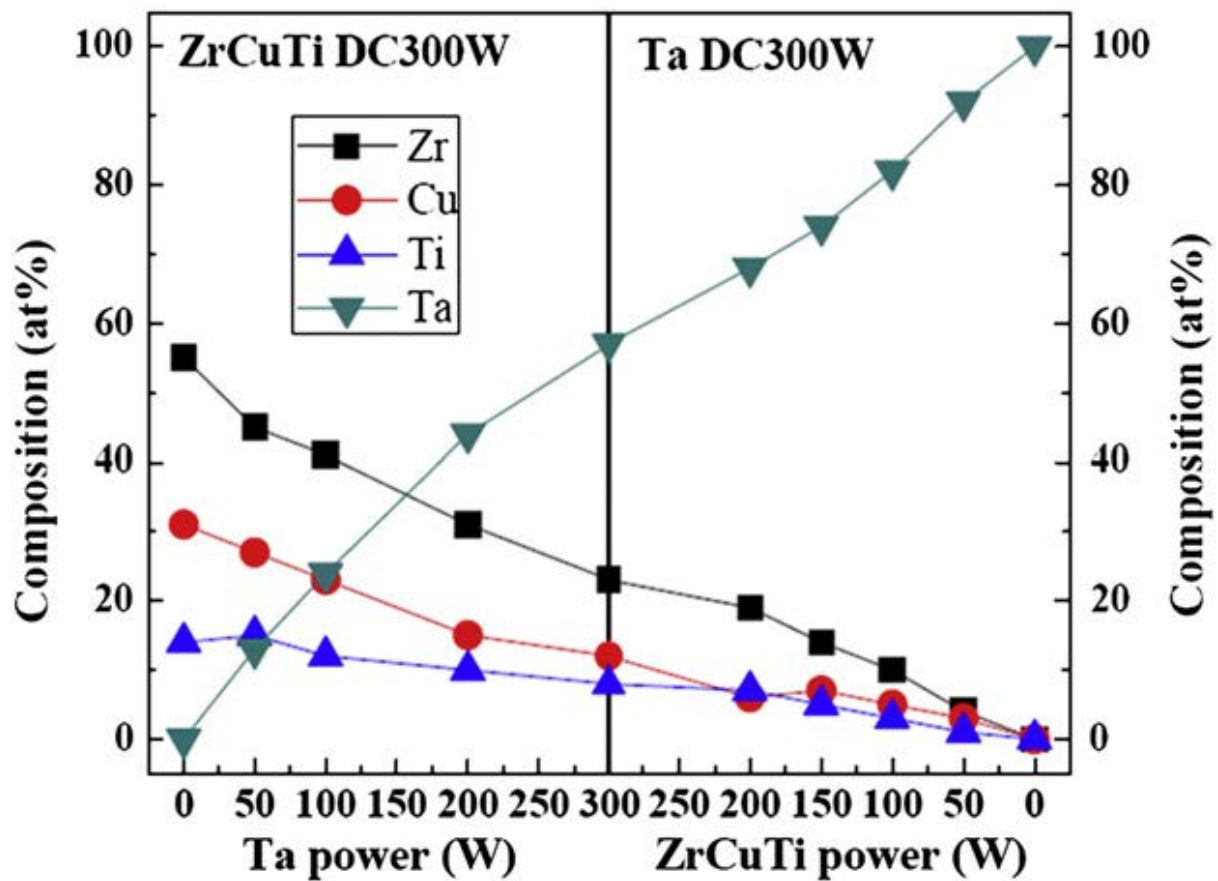
Figure 3-1   The variation of thin film compositions of the ZrCuTi-Ta TFMGs as a

function of two DC gun powers.
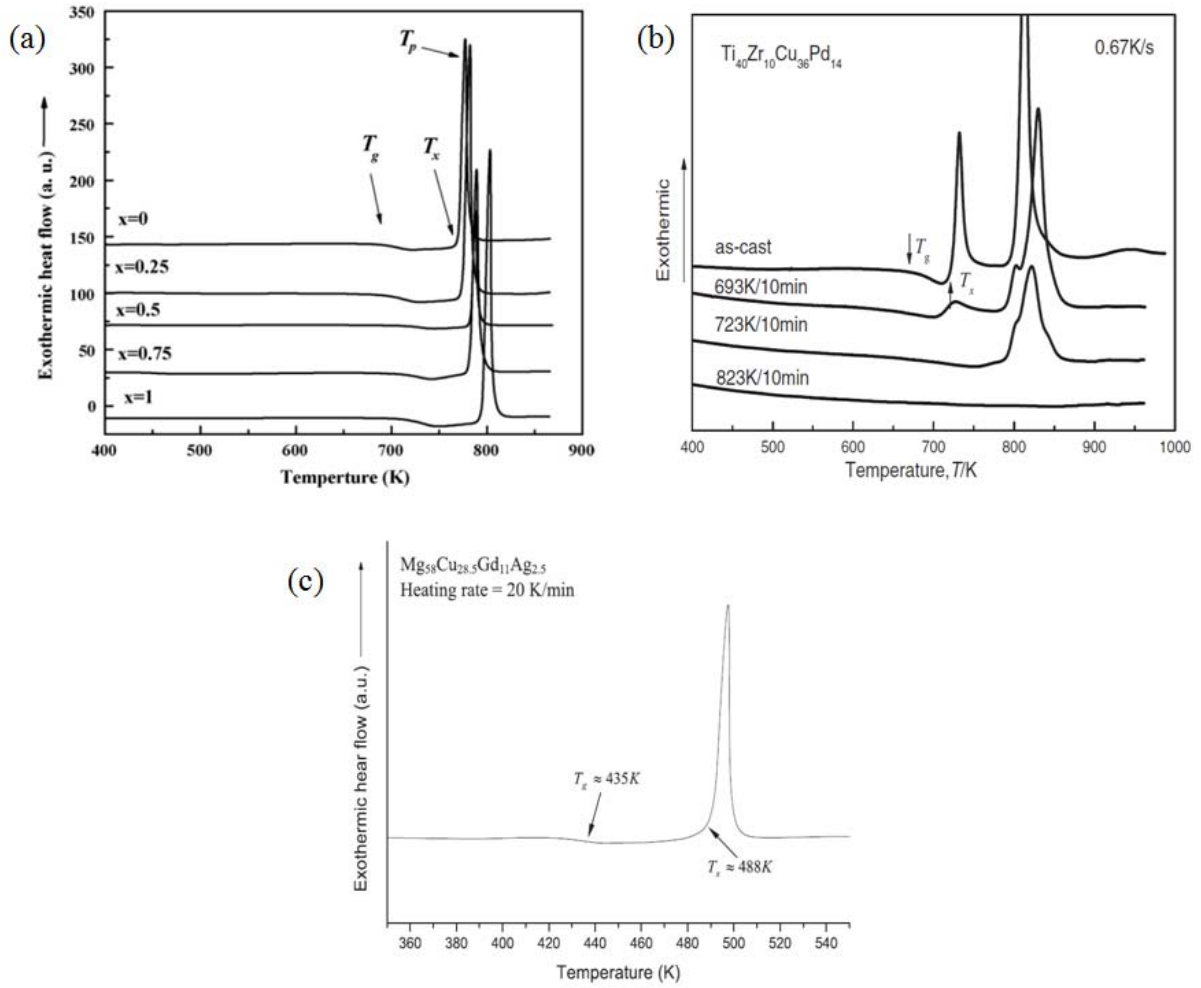
Figure 3-2   (a) DSC plots of $(Zr_{53}Cu_{30}Ni_9Al_8)_{100-x}Si_x$ amorphous alloys. (b) DSC curves

of the $Ti_{40}Cu_{36}Pd_{14}Zr_{10}$ bulk metallic glass and its crystalline alloys. (c) DSC

trace of as-cast $Mg_{58}Cu_{28.5}Gd_{11}Ag_{2.5}$ alloy.
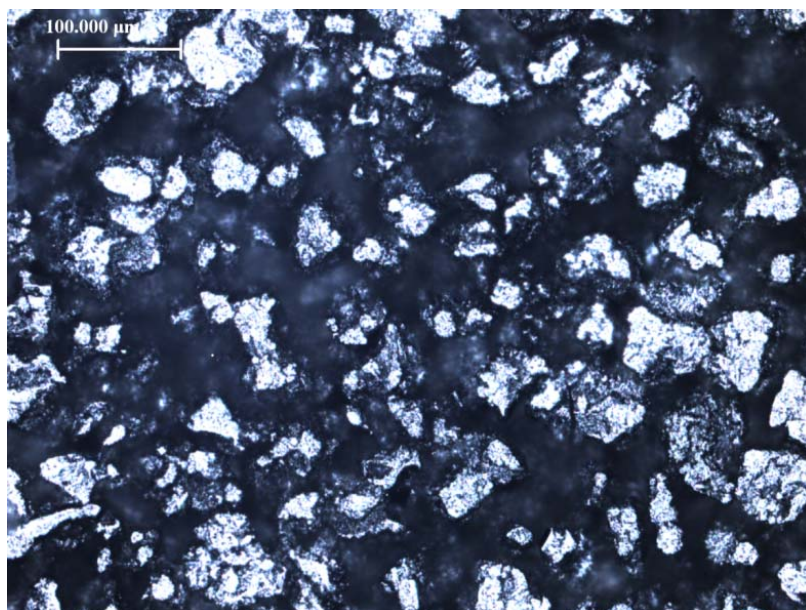
Figure 3-3   The OM image of the cold pressed $Mg_{58}Cu_{28.5}Gd_{11}Ag_{2.5}$ and $Zr_{53}Cu_{30}Ni_9Al_8$

powders without heat treatment.
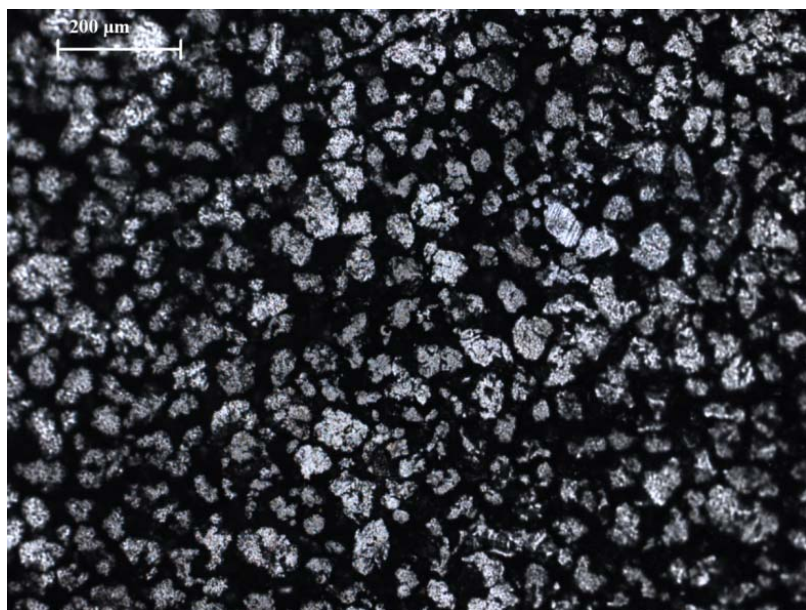
Figure 3-4   The OM image of the pressed $Mg_{58}Cu_{28.5}Gd_{11}Ag_{2.5}$ and $Zr_{53}Cu_{30}Ni_9Al_8$

powders after heat treatment in TMA at 180^oC.
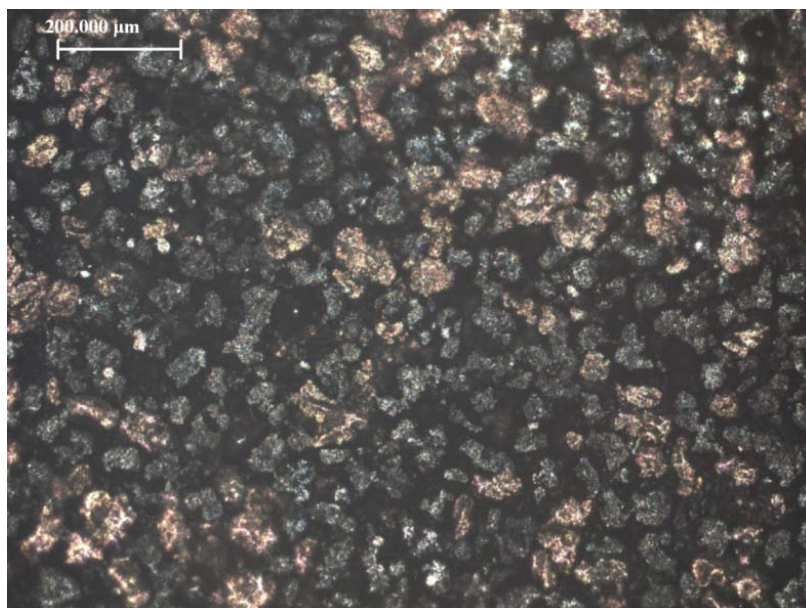
Figure 3-5   The OM image of the pressed $Mg_{58}Cu_{28.5}Gd_{11}Ag_{2.5}$ and $Zr_{53}Cu_{30}Ni_9Al_8$

powders after heat treatment in TMA at 395^oC.
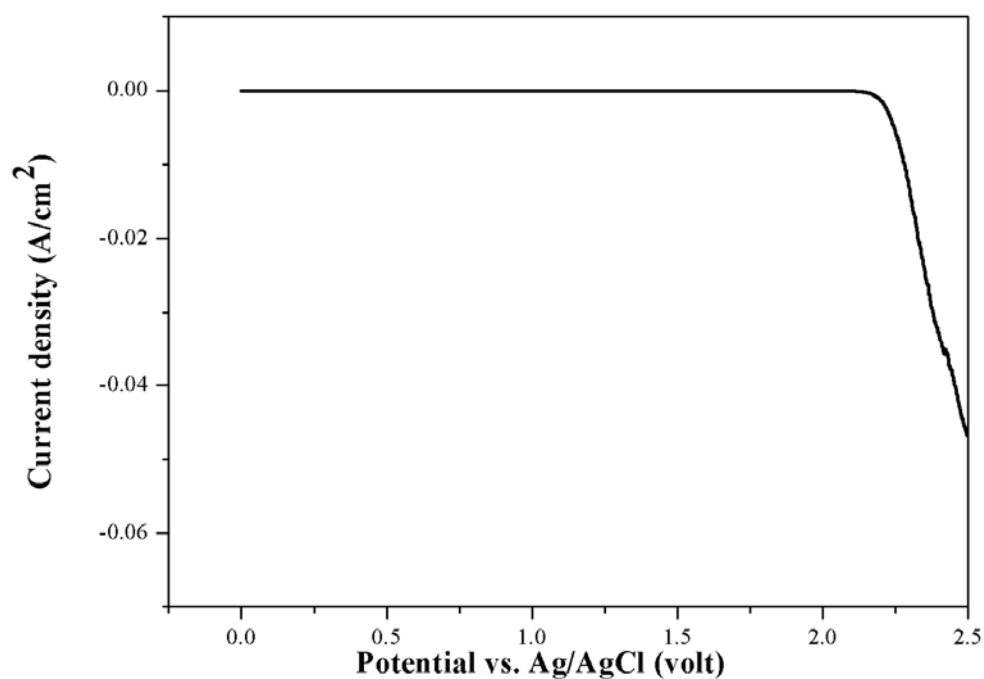
Figure 3-6   The anodic polarization of $Zr_{53}Cu_{30}Ni_9Al_8$ ribbon for the determination of E_c.
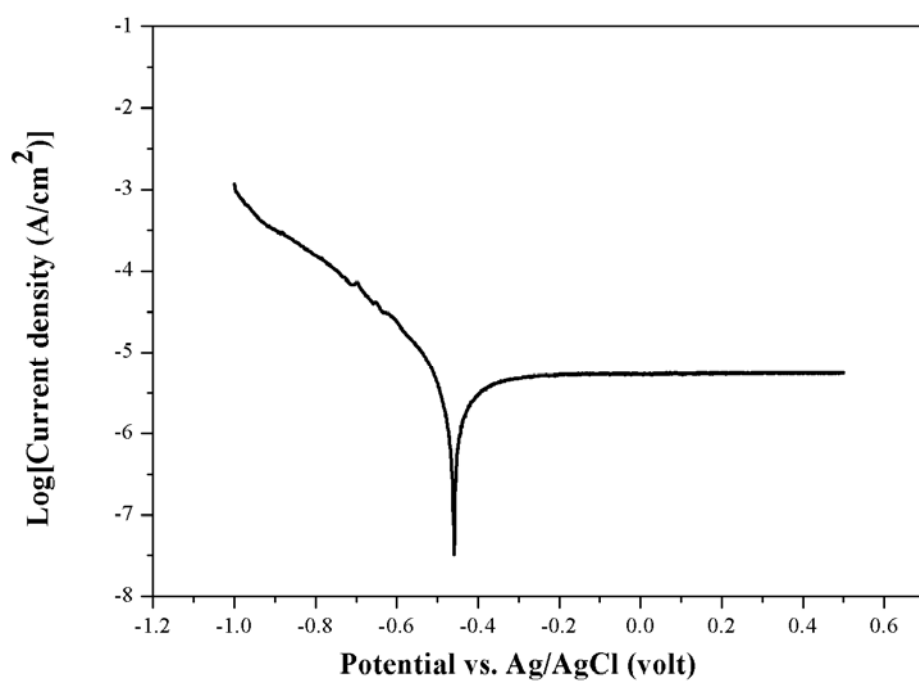
Figure 3-7   The tafel slope of $Zr_{53}Cu_{30}Ni_9Al_8$ ribbons for the determination of I_{corr} and E_{corr}.
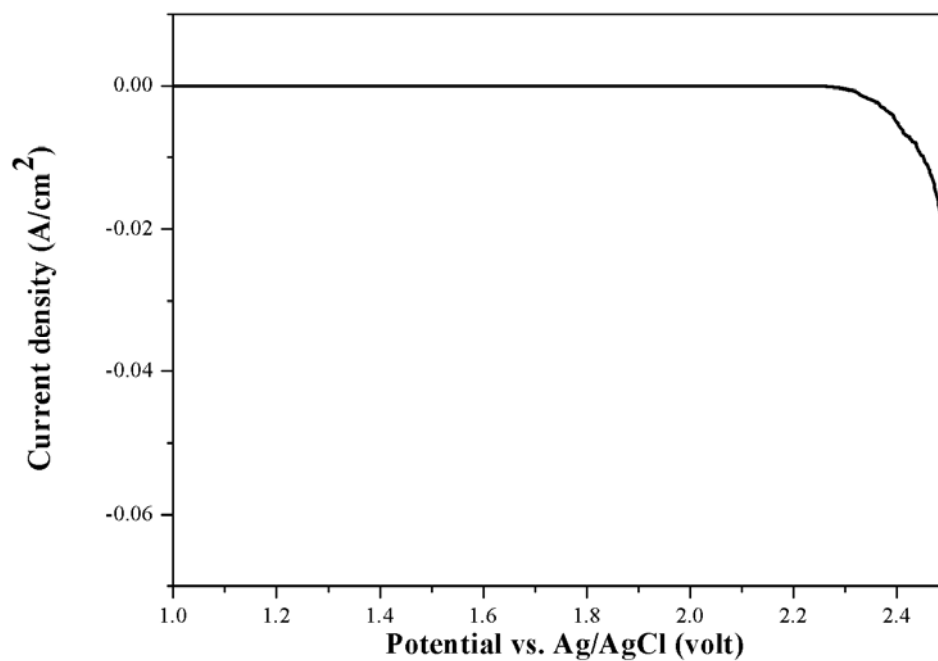
Figure 3-8   The anodic polarization of $Mg_{58}Cu_{28.5}Gd_{11}Ag_{2.5}$ powders for the determination

of E_c.
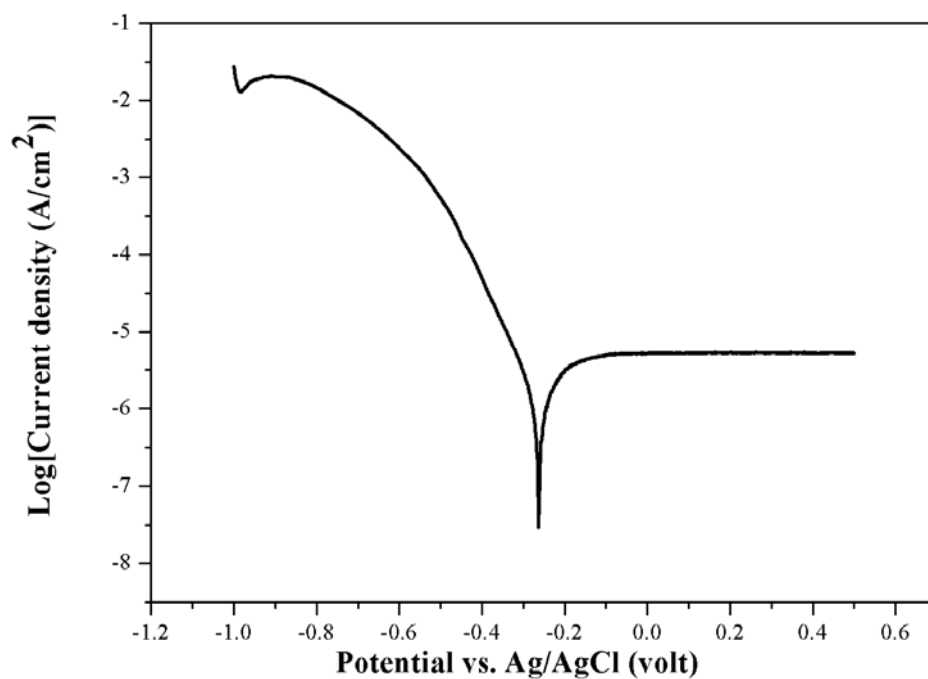
Figure 3-9   The tafel slope of $Mg_{58}Cu_{28.5}Gd_{11}Ag_{2.5}$ ribbons for the determination of I_{corr}

and E_{corr}.
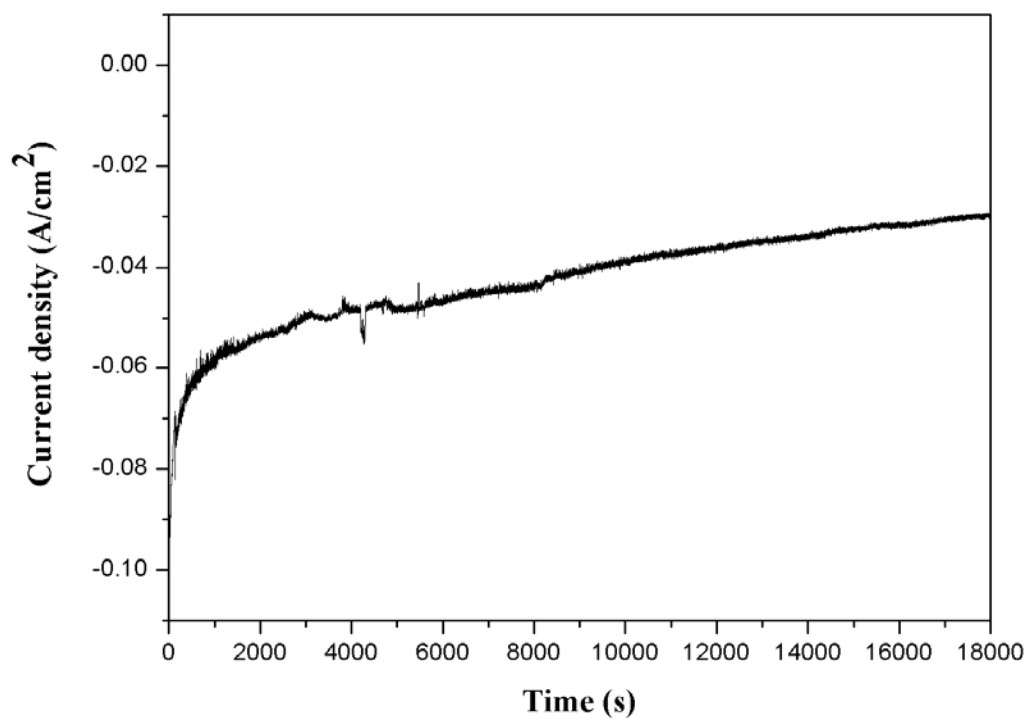
Figure 3-10 The i-t curve of sintered $Zr_{53}Cu_{30}Ni_9Al_8$ and $Ti_{40}Cu_{36}Pd_{14}Zr_{10}$ MG powder

sample at 2.3 V.
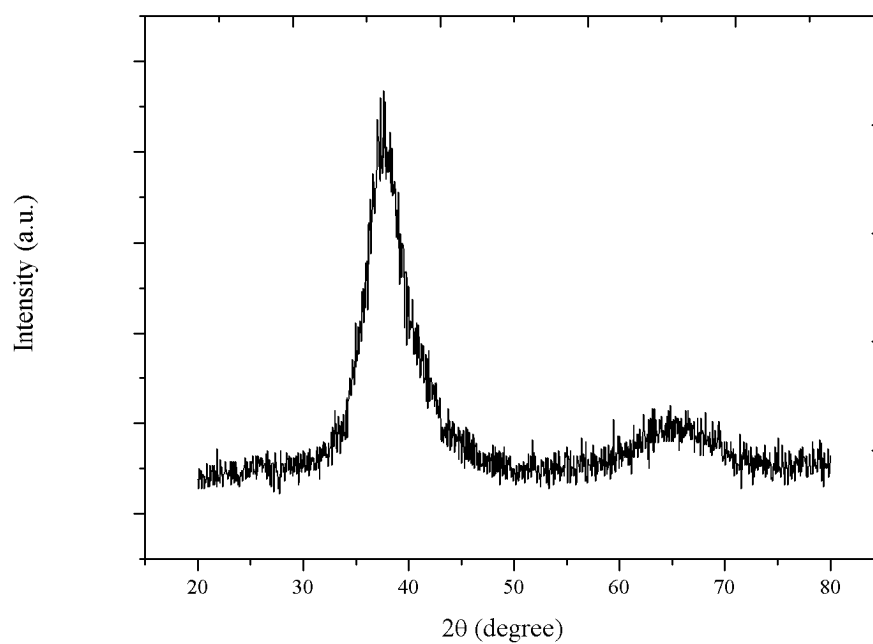
Figure 3-11   The XRD pattern of Ta$_{57}$Zr$_{23}$Cu$_{12}$Ti$_8$ thin film.
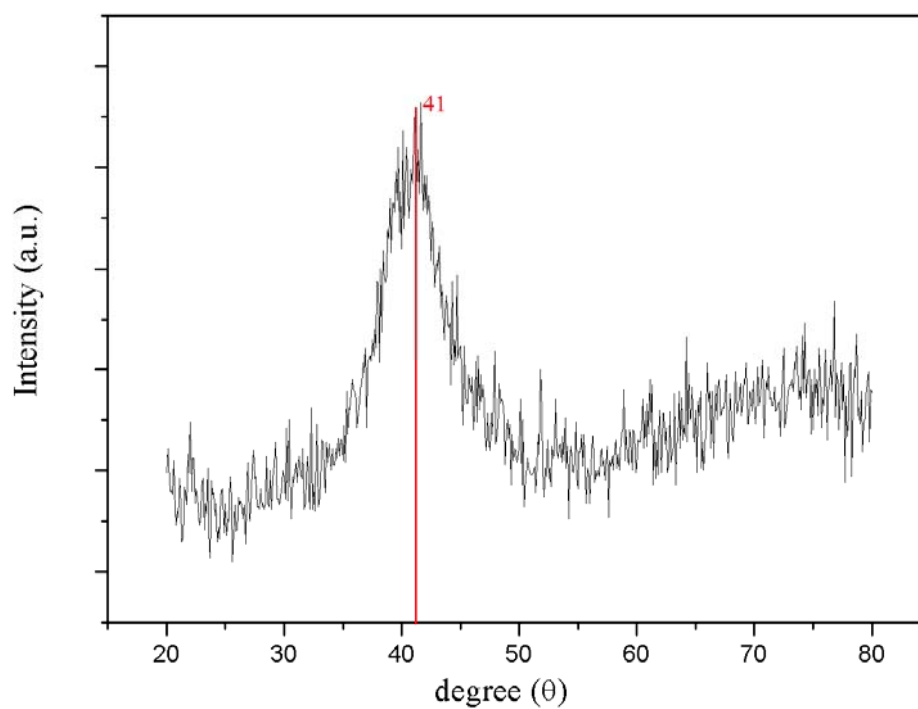
Figure 3-12   The XRD pattern of Ti$_{40}$Cu$_{36}$Pd$_{14}$Zr$_{10}$ amorphous powders.
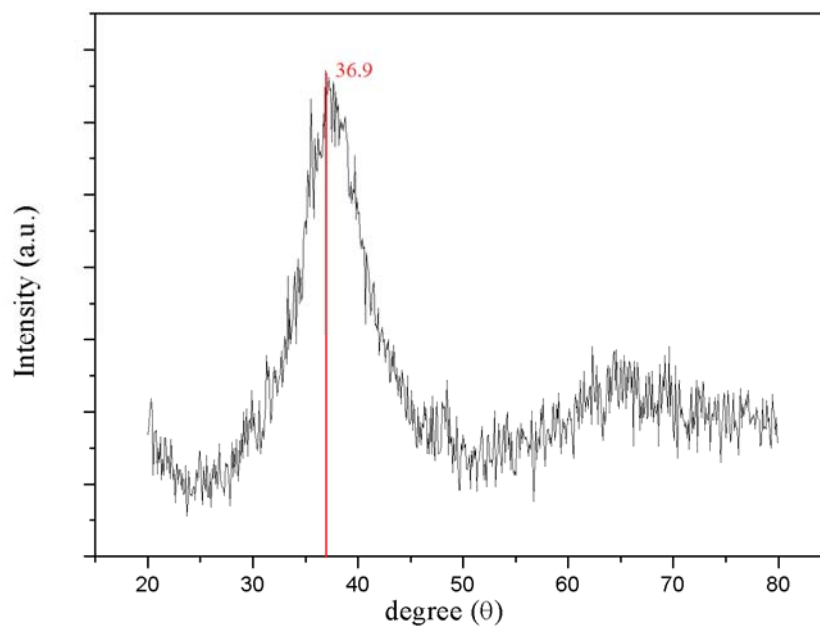
Figure 3-13   The XRD pattern of $Zr_{53}Cu_{30}Ni_9Al_8$ amorphous powders.
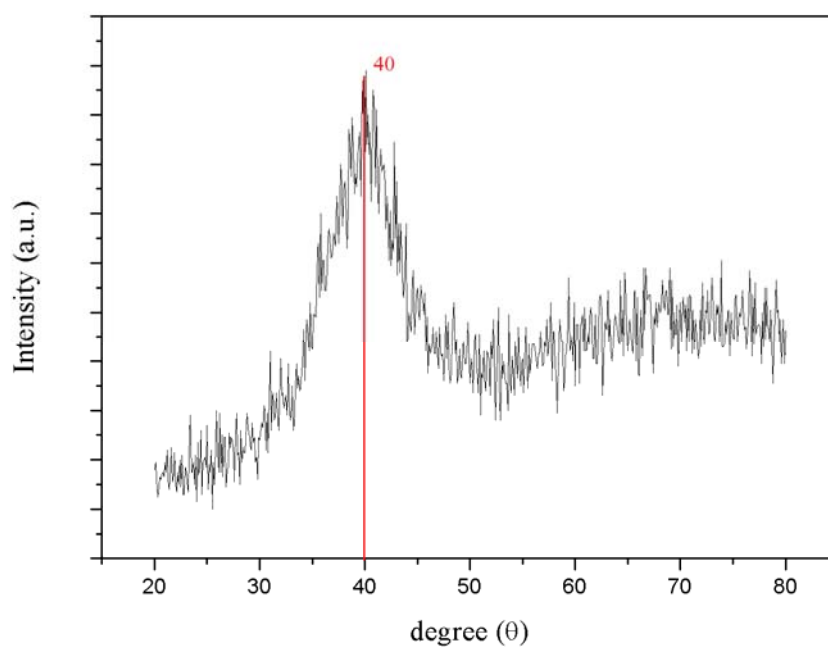
Figure 3-14   The XRD pattern of the mixed powders after sintering at $410^{o}C$ for 10 min of

the Zr- and Ti-based MG powders

81
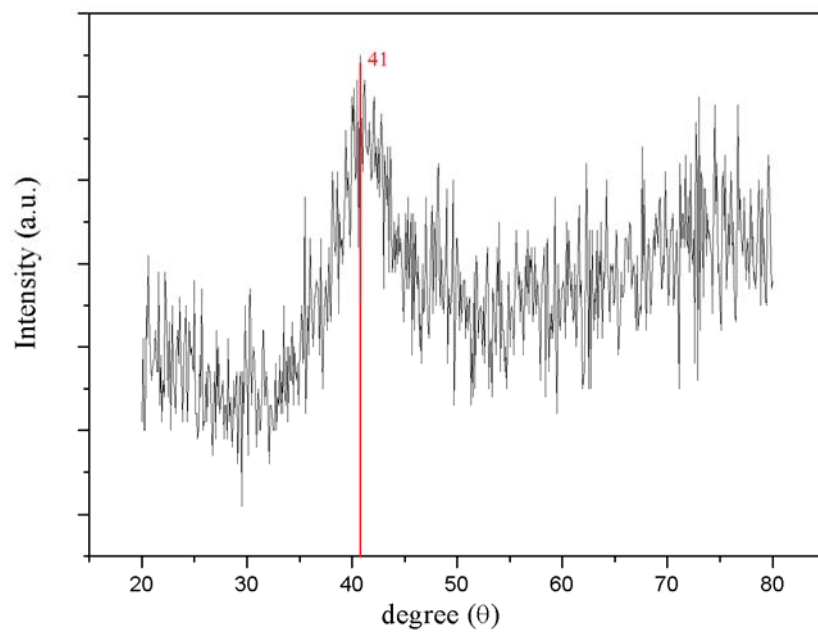
Figure 3-15   The XRD pattern of the sintered specimens that had been immersed in solution

for dealloying.
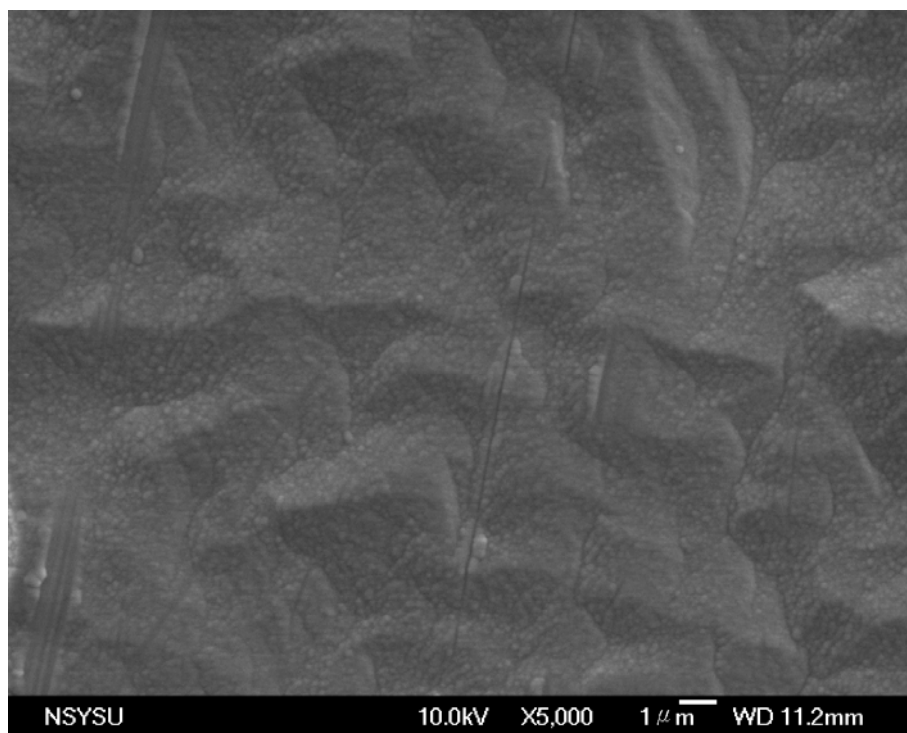
Figure 3-16   SEM micrpgraph showing the surface morphology of $Ta_{57}Zr_{23}Cu_{12}Ti_8$ thin

film, without etching, at 5000X.
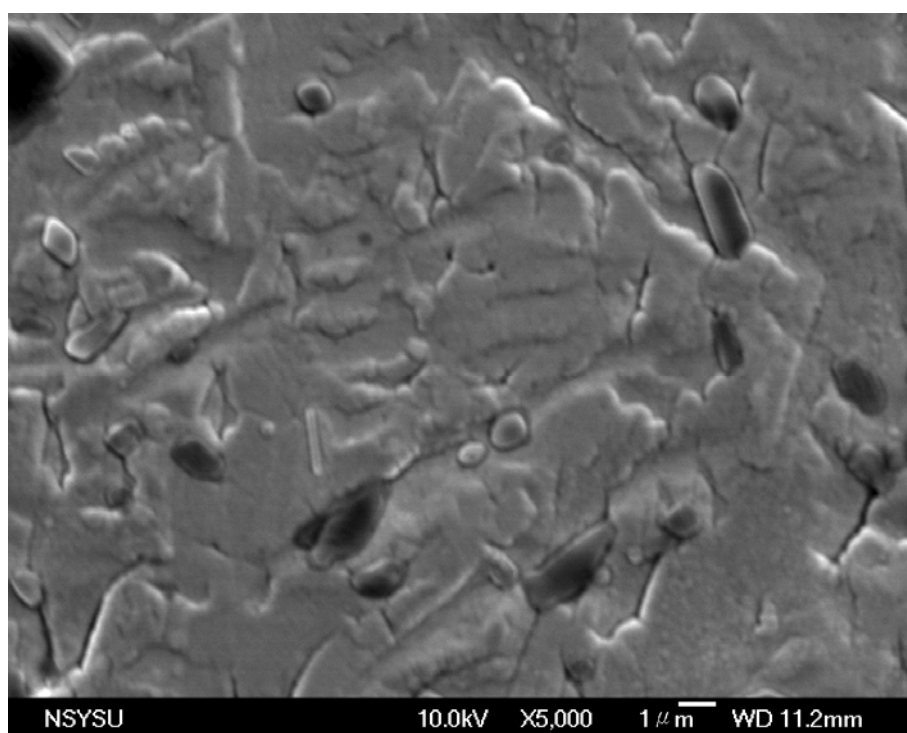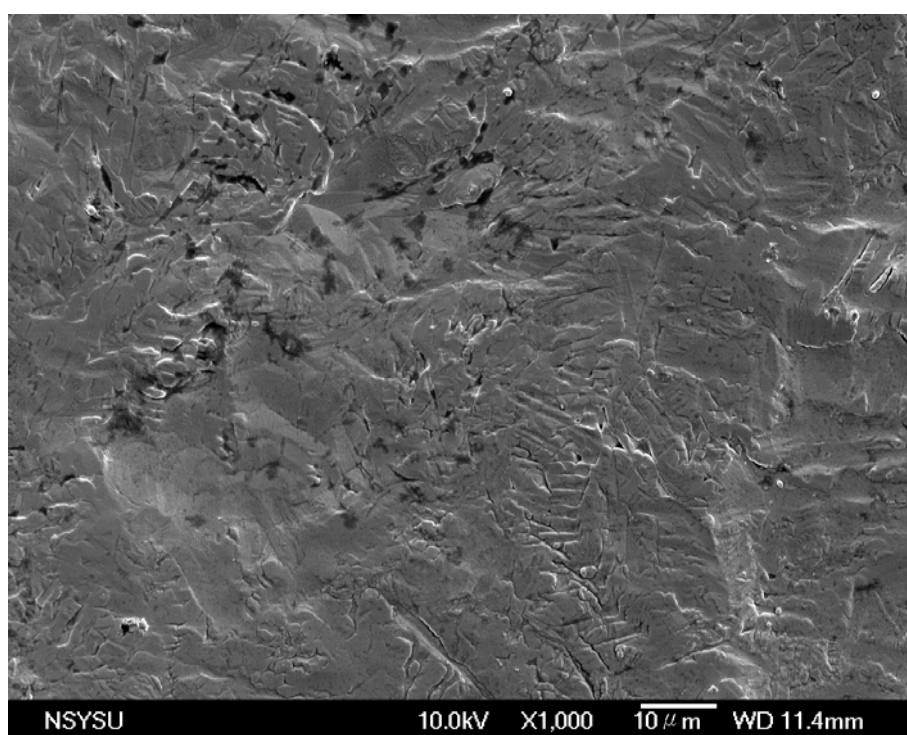
Figure 3-17   Surface morphology of $Ta_{57}Zr_{23}Cu_{12}Ti_8$ thin film, etching in 0.1 M $H_2SO_{4(aq)}$

with 3 V, at 1000X and 5000X.

(a)

(b)

(c)

NSYSU   10.0kV   X500   10 μm   WD 11.2mm

(d)

NSYSU   10.0kV   X500   10 μm   WD 11.2mm
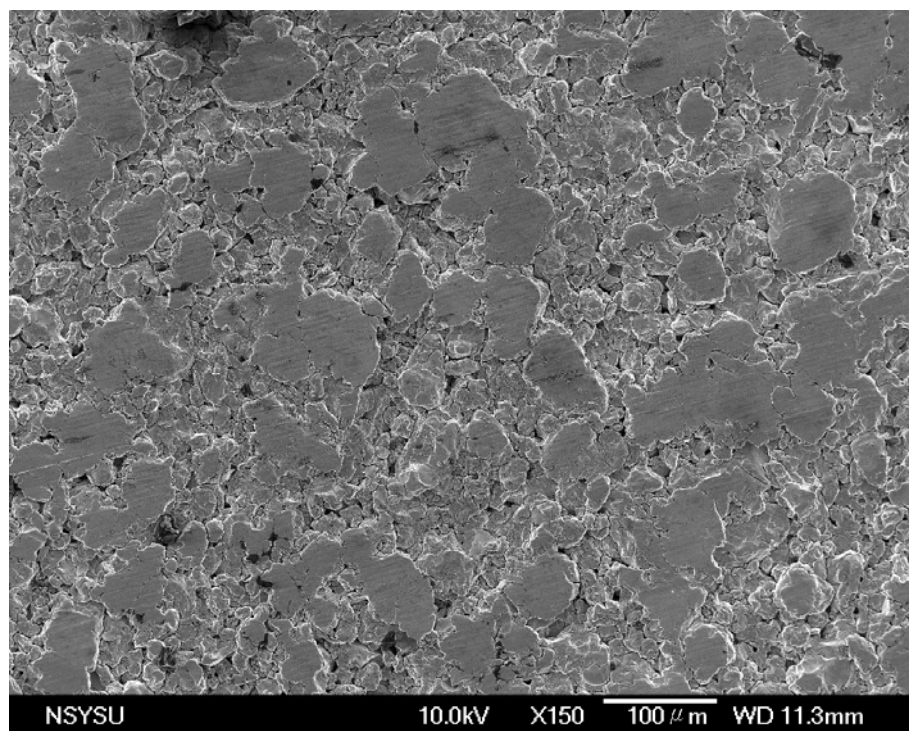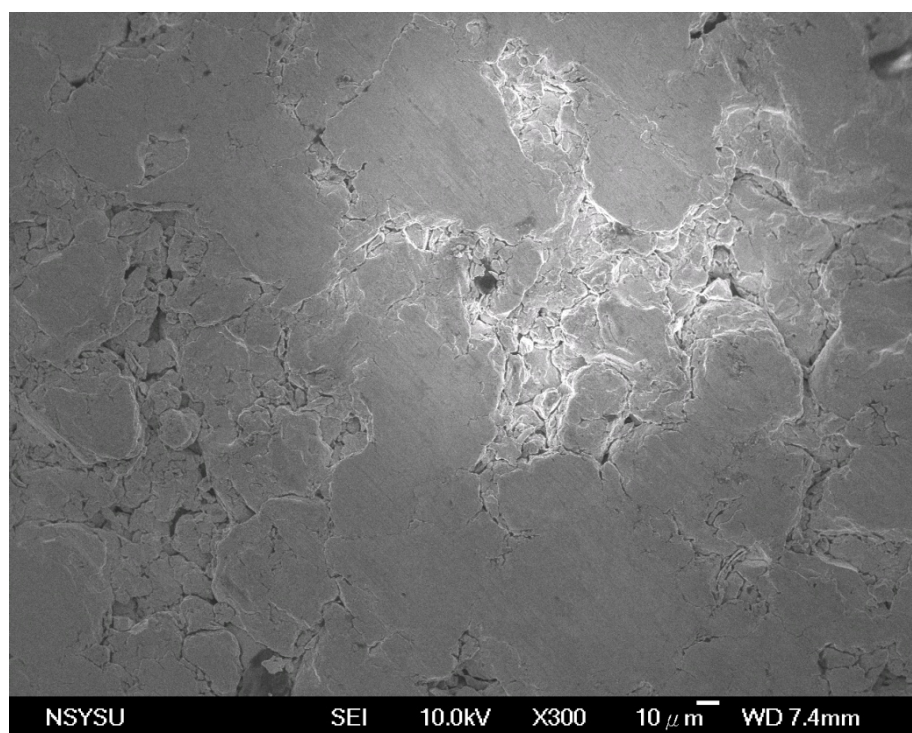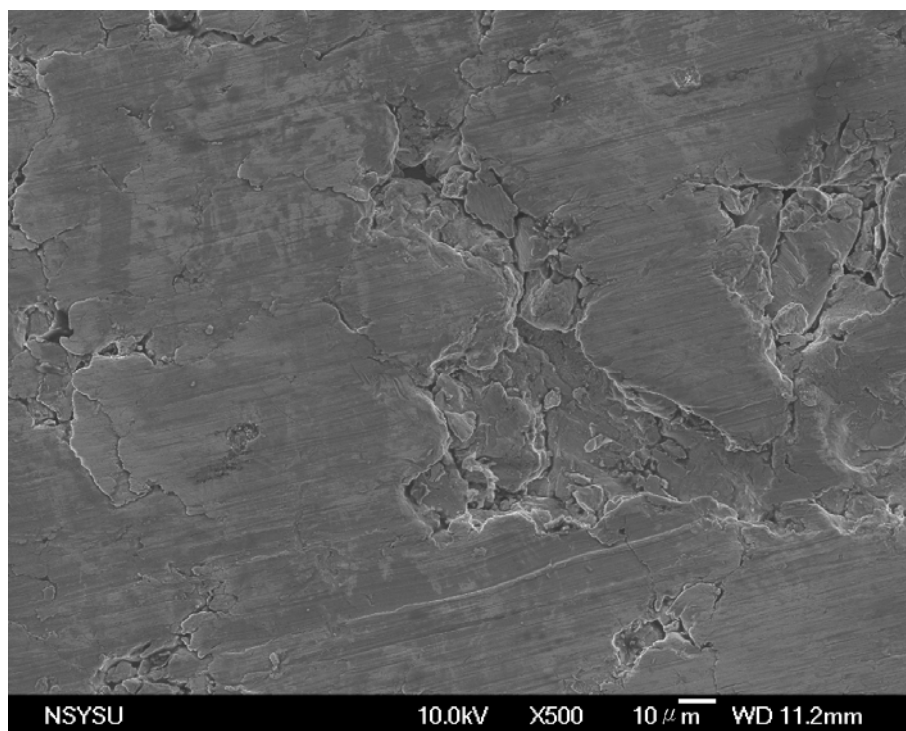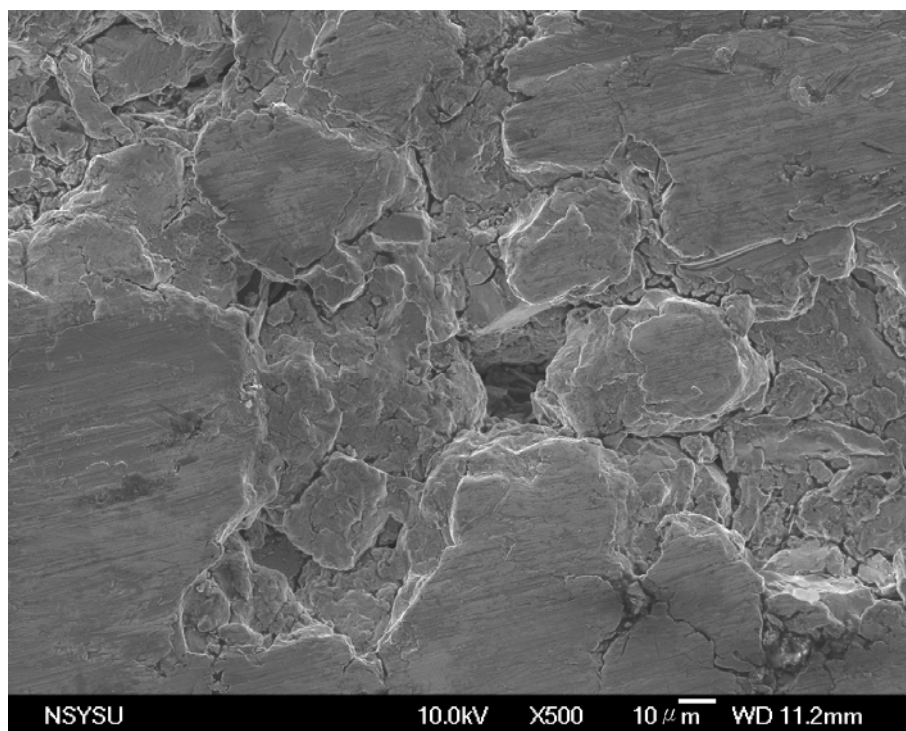
Figure 3-18   Surface morphology of the mixed powders after sintering at 410°C for 10 min

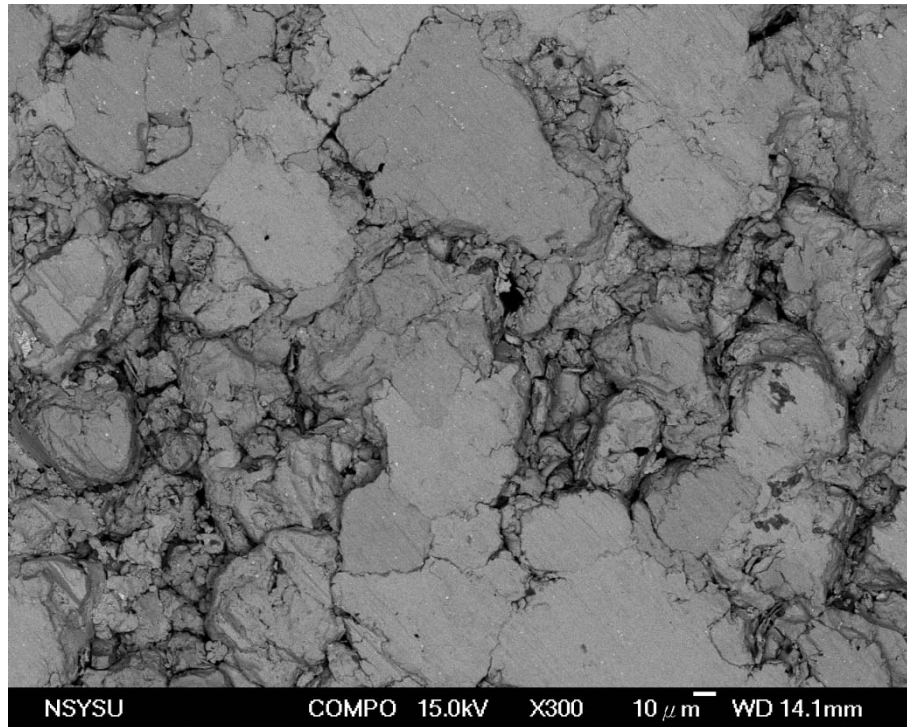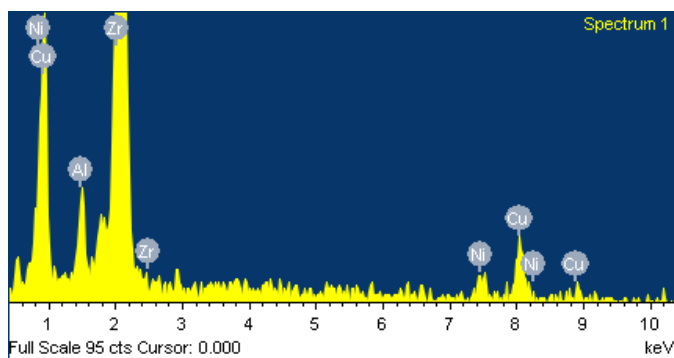of the Zr- and Ti-based MG powders at different SEM magnification.

86

Figure 3-19   The BEI image of the mixed powders after sintering at 410$^{\text{o}}$C for 10 min of the

Zr- and Ti-based MG powders.

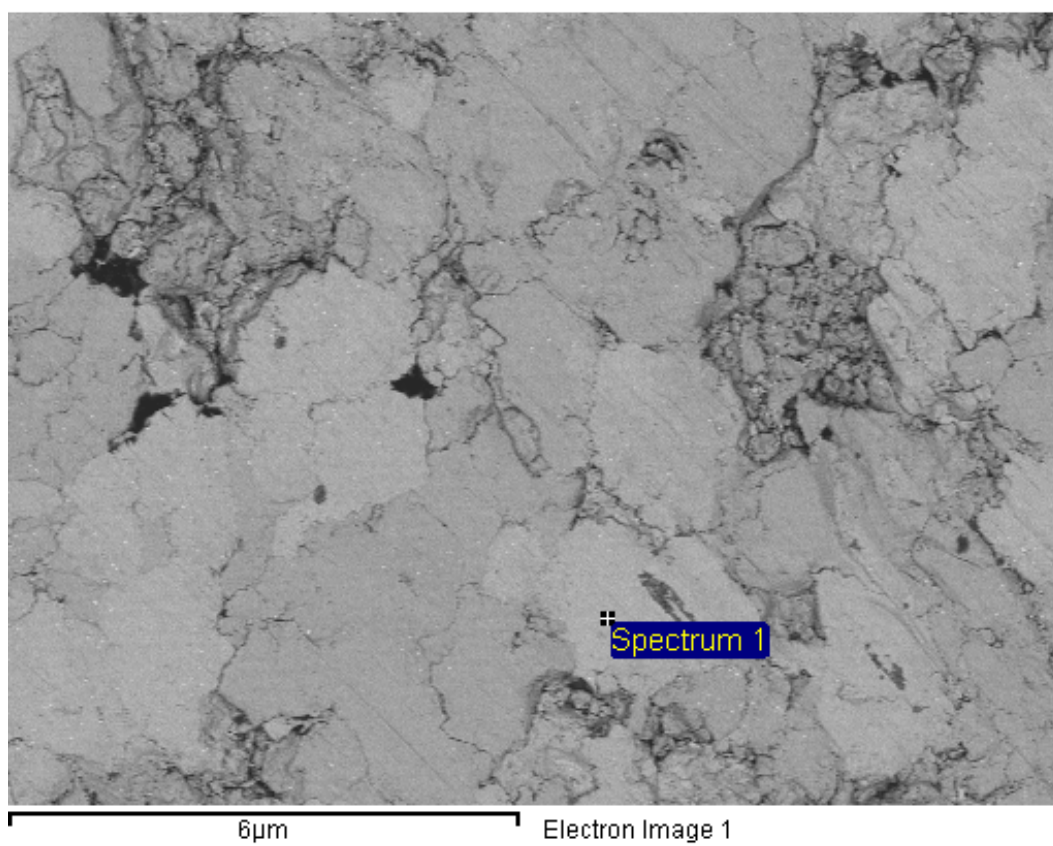| Element	Weight%	Atomic%
Al K	2.54	7.37
Ni L	3.64	4.86
Cu L	19.13	23.60
Zr L	74.69	64.18
Totals	100.00	

Figure 3-20   The EDS result of the bright zone in the BEI image.

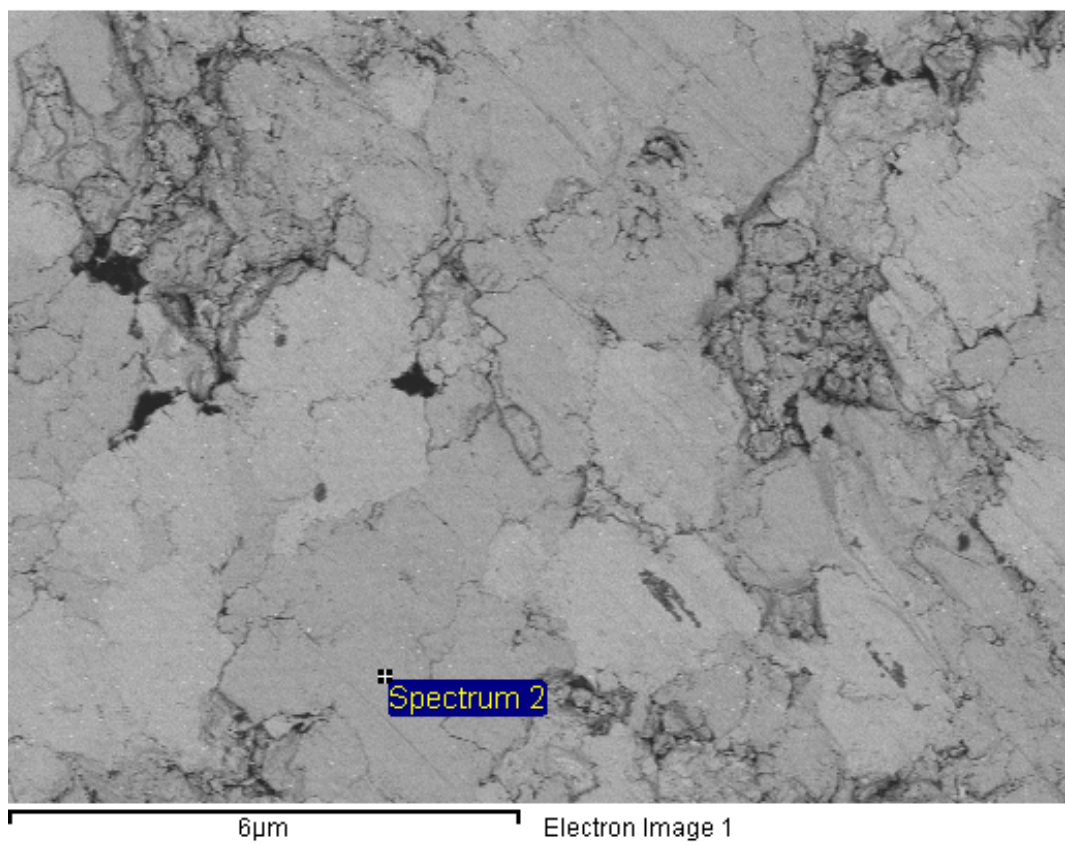| Element	Weight%	Atomic%
Ti K	43.15	56.85
Cu L	20.58	20.44
Zr L	12.11	8.38
Pd L	24.16	14.33
Totals	100.00	
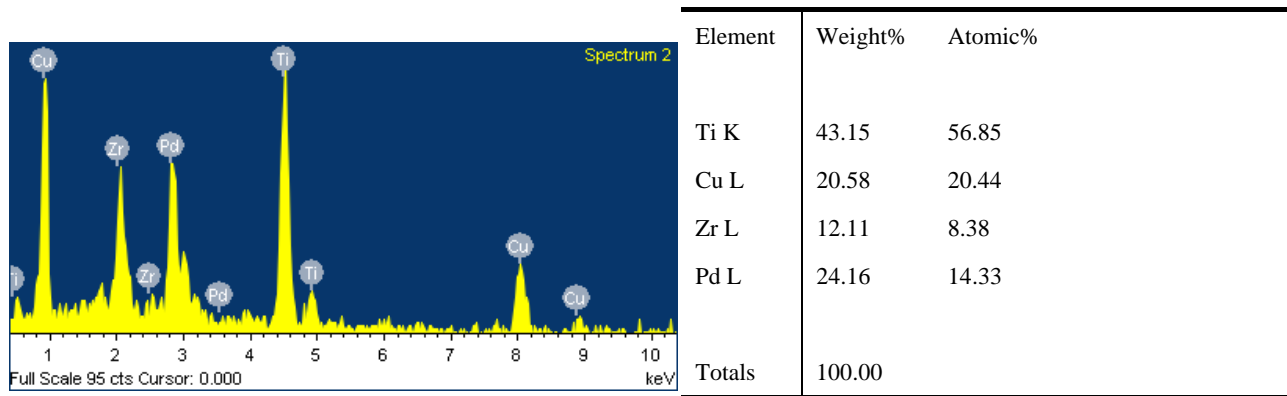
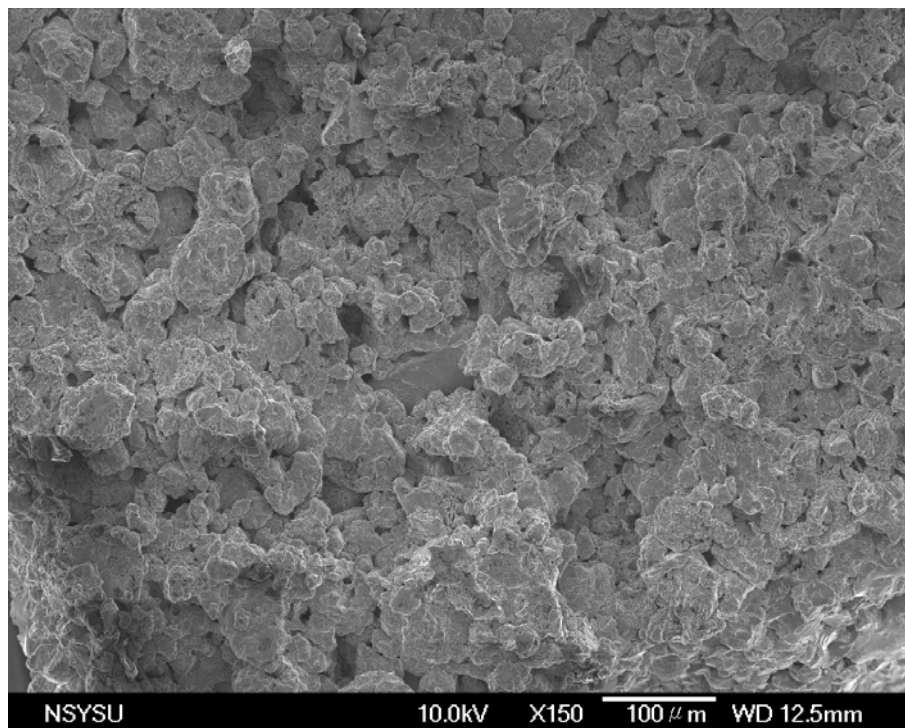**Figure 3-21** The EDS result of the dark zone in the BEI image.

(a)

(b)

(c)

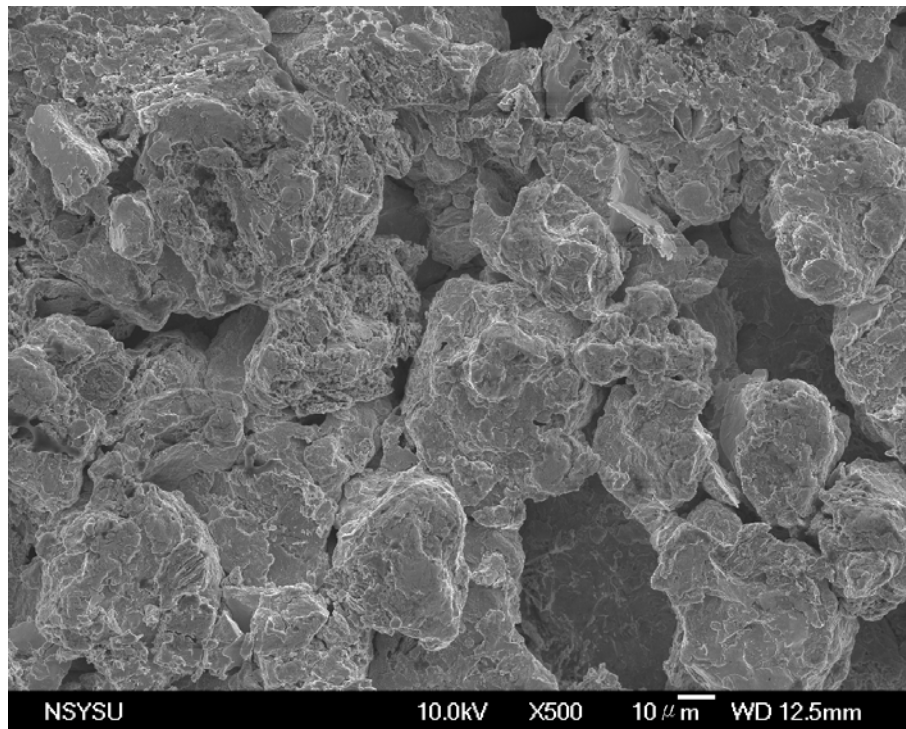NSYSU   10.0kV   X500   10 μ m   WD 12.5mm
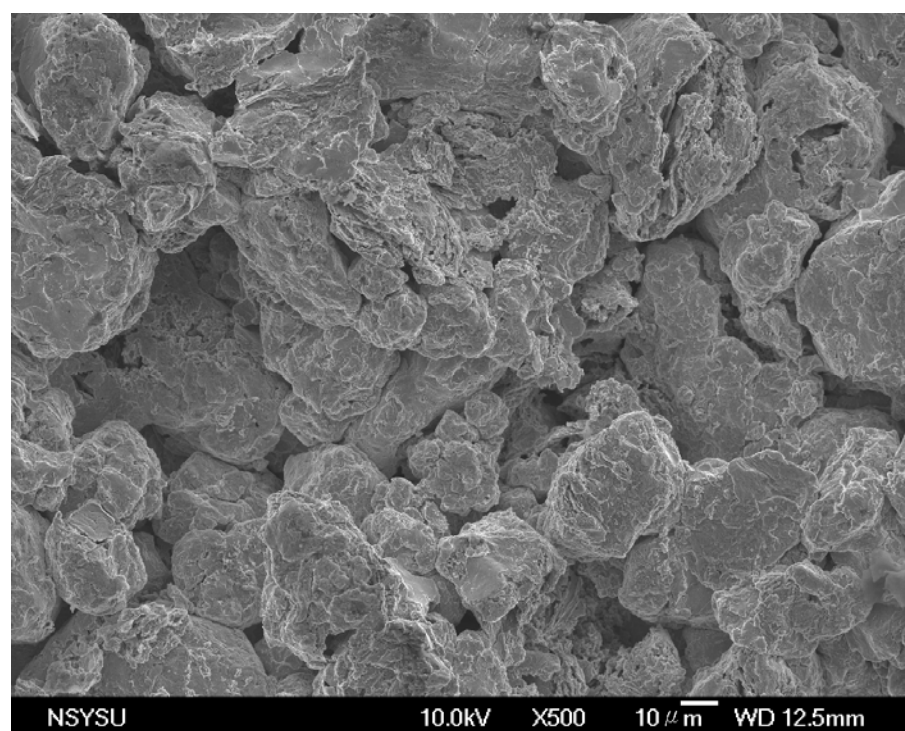
Figure 3-22   Surface morphology of the Zr- and Ti-based sintered specimens after the

etching or dealloying process in HNO_3 for 5 hours at different SEM
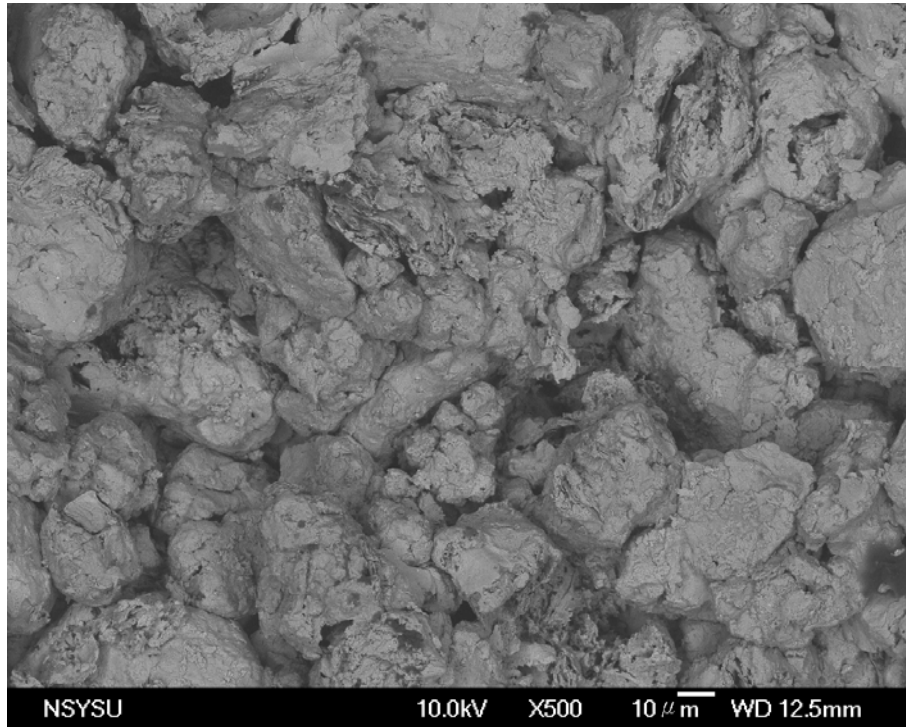
magnification..

Figure 3-23   The BEI image of the Zr- and Ti-based sintered specimens after the etching or

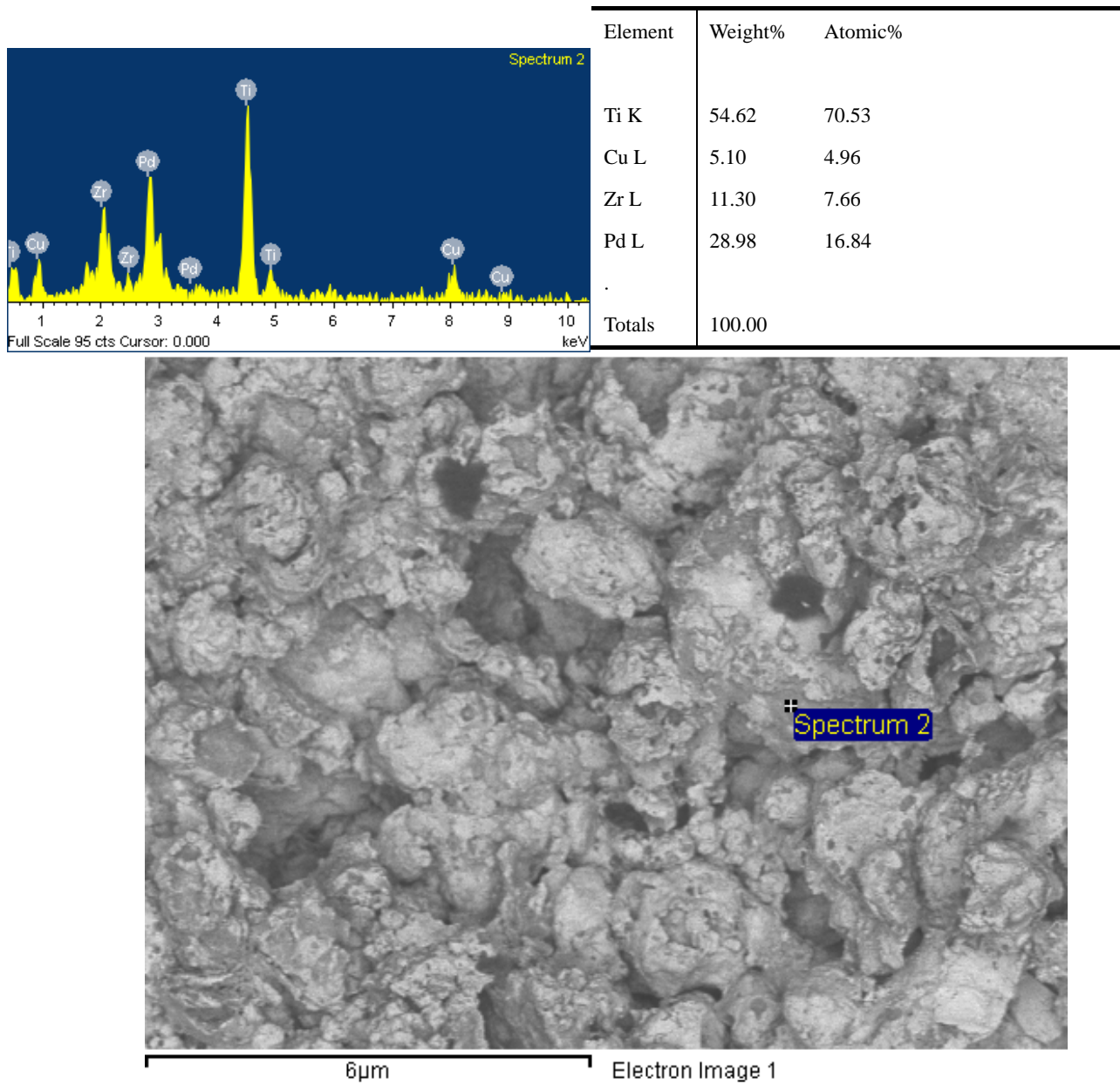dealloying process in HNO_3 for 5 hours.

Element	Weight%	Atomic%
Ti K	54.62	70.53
Cu L	5.10	4.96
Zr L	11.30	7.66
Pd L	28.98	16.84
.		
Totals	100.00	

Figure 3-24   The EDS result of the Zr- and Ti-based sintered specimens after the etching or

dealloying process.

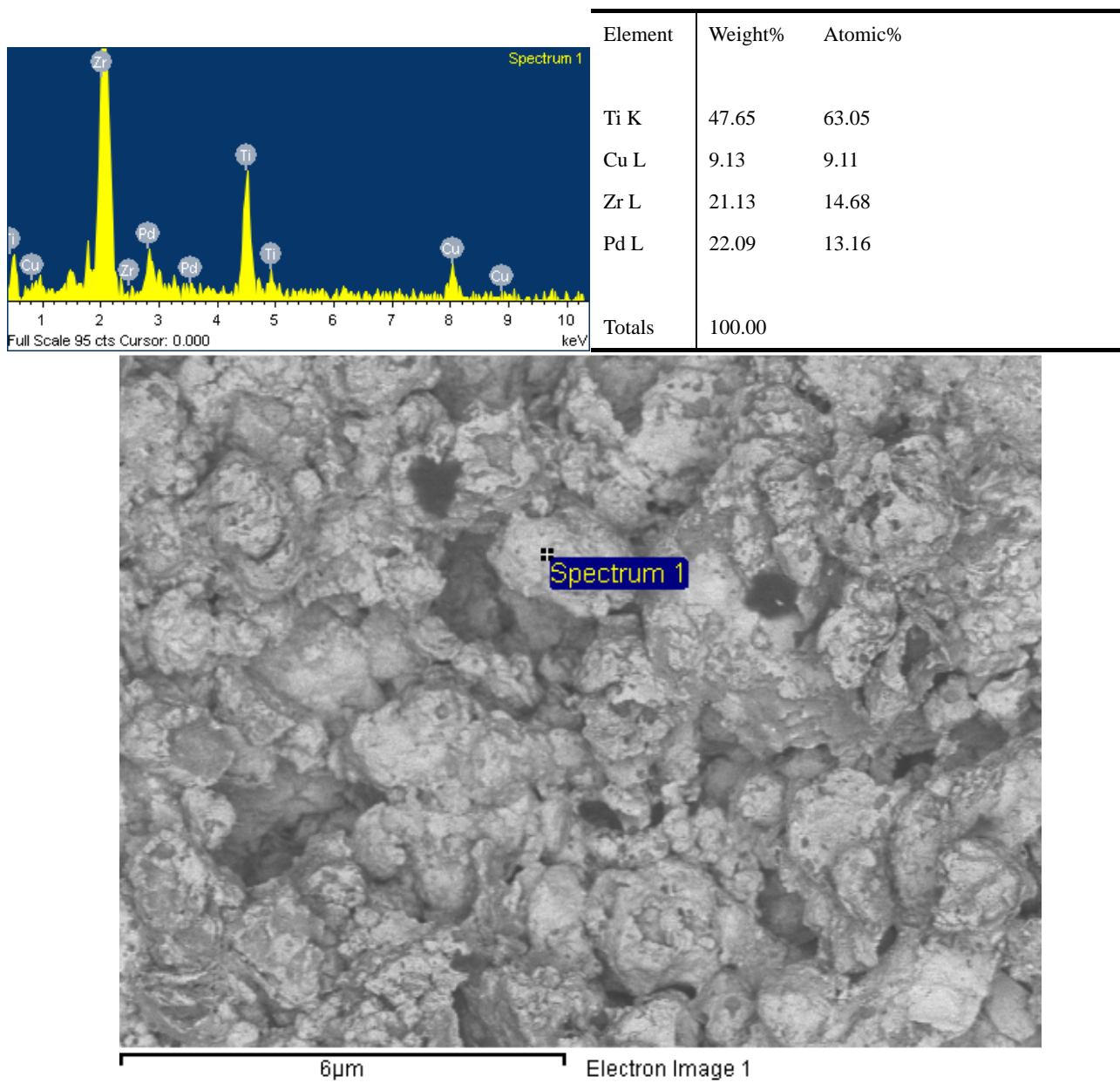| Element	Weight%	Atomic%
Ti K	47.65	63.05
Cu L	9.13	9.11
Zr L	21.13	14.68
Pd L	22.09	13.16
Totals	100.00	

Figure 3-25   The EDS result of the Zr- and Ti-based sintered specimens after the etching or

dealloying process.

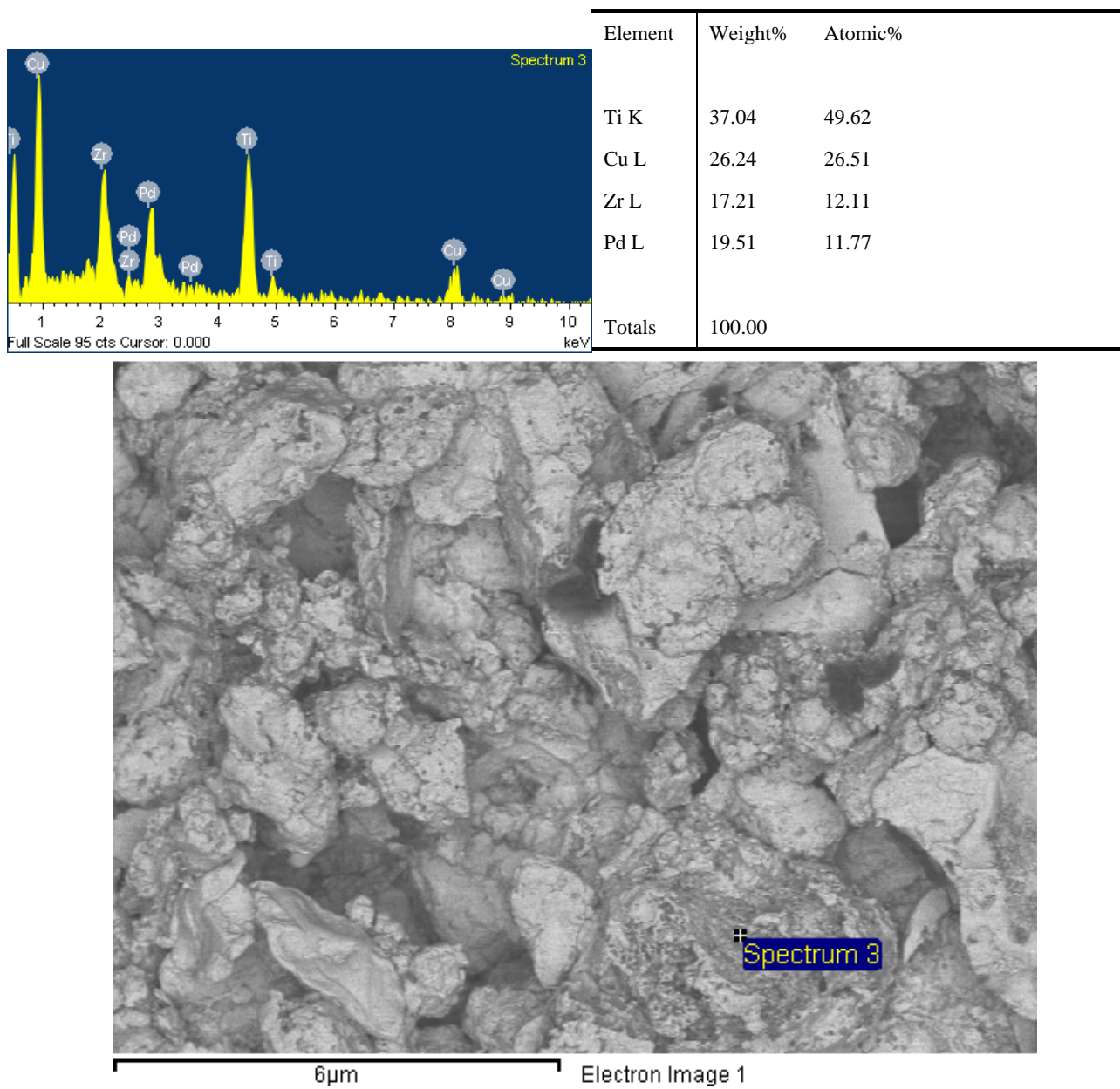| Element	Weight%	Atomic%
Ti K	37.04	49.62
Cu L	26.24	26.51
Zr L	17.21	12.11
Pd L	19.51	11.77
Totals	100.00	

Figure 3-26   The EDS result of the Zr- and Ti-based sintered specimens after the etching or

dealloying process.

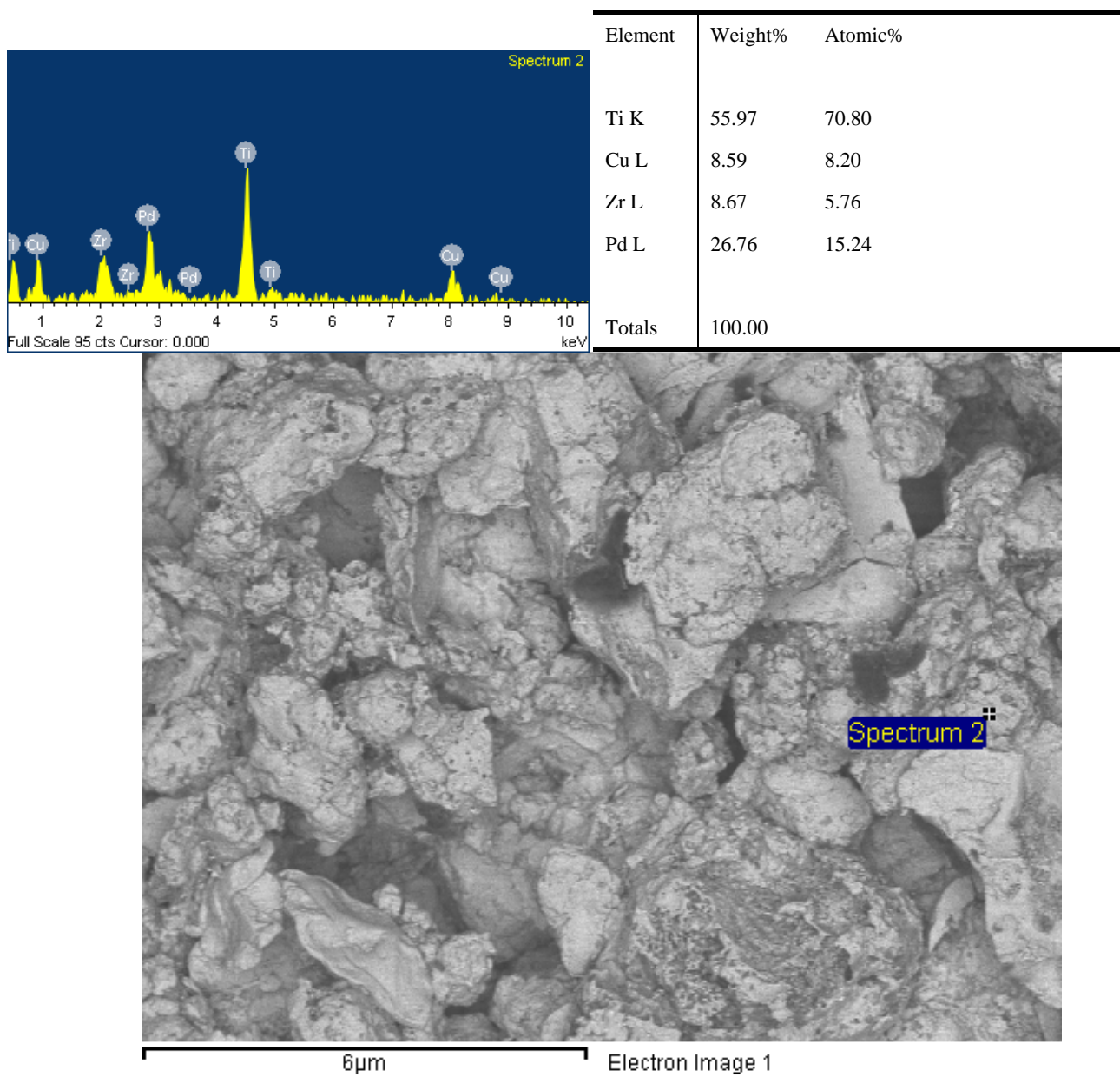| Element	Weight%	Atomic%
Ti K	55.97	70.80
Cu L	8.59	8.20
Zr L	8.67	5.76
Pd L	26.76	15.24
Totals	100.00	

Figure 3-27 The EDS result of the Zr- and Ti-based sintered specimens after the etching or
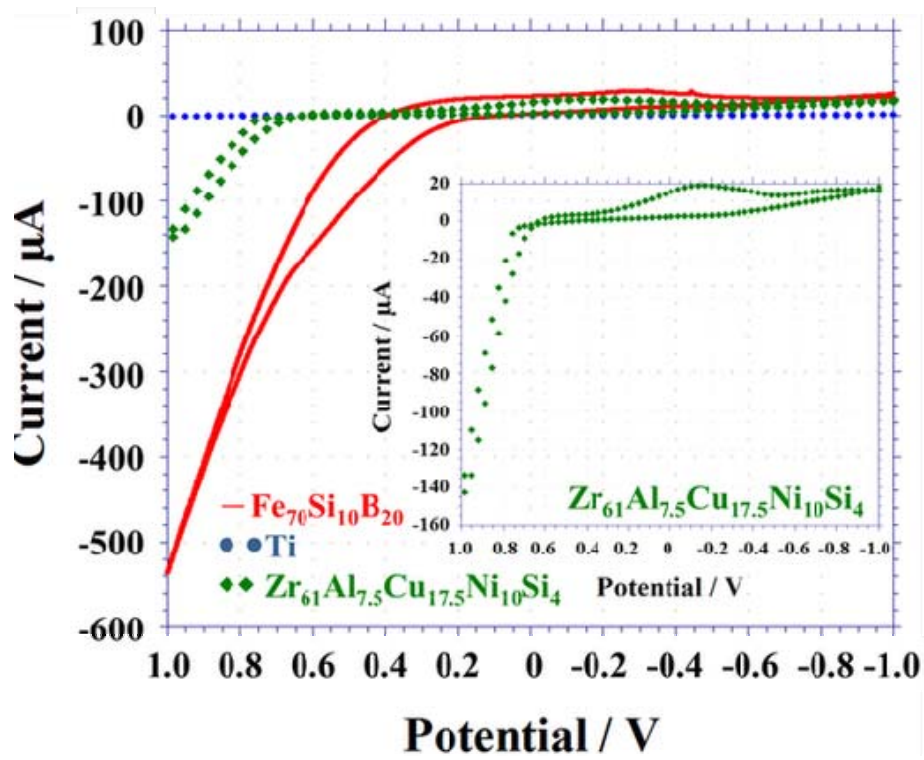
dealloying process.

Figure 3-28 The comparison of cyclic voltammograms for various MGs and pure Ti in Hank's solution. In the inset shows the cyclic voltammograms of $Zr_{61}Cu_{17.5}Ni_{10}Al_{7.5}Si_4$ only.